

# On the Threshold of Drop Fragmentation under Impulsive Acceleration

Aditya Parik<sup>1†</sup>, T. Truscott<sup>2</sup>, and S. Dutta<sup>1‡</sup>

<sup>1</sup>Department of Mechanical and Aerospace Engineering,  
Utah State University, UT 84321, USA

<sup>2</sup>Department of Mechanical Engineering,  
King Abdullah University of Science and Technology, Saudi Arabia

(Received xx; revised xx; accepted xx)

Secondary fragmentation of an impulsively accelerated drop depends on fluid properties and velocity of the ambient. The critical Weber number ( $We_{cr}$ ), the minimum Weber number at which a drop undergoes non-vibrational breakup, depends on fluid density ratio ( $\rho$ ), the drop ( $Oh_d$ ), and the ambient ( $Oh_o$ ) Ohnesorge numbers. The current study uses VoF based interface-tracking multiphase flow simulations to quantify the effect of different non-dimensional groups on the threshold at which secondary fragmentation occur. For  $Oh_d \leq 0.1$ , a decrease in  $Oh_d$  significantly influences the breakup morphology, plume formation, and the resulting  $We_{cr}$ .  $\rho$  and  $Oh_o$ , were found to influence the balance between the pressure differences between the poles and the periphery, and the shear stresses on the upstream surface. These external forces induce flow inside the initially spherical drop, resulting in deformation into pancakes and eventually the breakup morphology of forward/backward bag. The evolution pathways of the drop morphology based on their non-dimensional groups have been charted. With the inclusion of the new observations, the traditional  $We_{cr} - Oh_d$  plot, used for illustrating the dependence of critical Weber number on  $Oh_d$ , was found to be inadequate in predicting the minimum initial  $We$  required to undergo fragmentation. A new non-dimensional parameter  $C_{breakup}$  is derived based on the competition between forces driving drop deformation and the forces resisting drop deformation. Tested on the available experimental data and current simulations,  $C_{breakup}$  is found to be a robust predictor for the threshold of drop fragmentation.

**Key words:** Drops, Threshold of Secondary Fragmentation, Impulsive acceleration

## 1. Introduction

Drop fragmentation, also known as secondary fragmentation, is the process of through which a drop breaks up under the action of external aerodynamic forces induced by the ambient flow. These forces originate due to a velocity deficit between the drop and the ambient medium. There are two fundamental ways a drop might experience a velocity deficit: a uniform ambient flow impacts a stationary drop in a gravity-free environment, called “impulsive acceleration” (Han & Tryggvason 2001); or an initially stationary drop accelerates under the action of a constant body force, while experiencing

† Email address for correspondence: aditya.parik@usu.edu

‡ Email address for correspondence: som.dutta@usu.edu

aerodynamic forces, called “free-fall” (Jalaal & Mehravaran 2012). For both cases, a liquid drop experiences aerodynamic forces that cause the drop to deform, which may lead to its fragmentation at a Weber number  $We_0$  higher than the critical value  $We_{cr}$  (Hinze 1949, 1955). During free-fall, the drop starts with zero aerodynamic forces that gradually increase to a maximum, at either its terminal or its breakup velocity. On the other hand, an impulsively accelerated drop starts its deformation process with the largest velocity deficit, and the corresponding large aerodynamic stresses acting on it. These stresses gradually reduce as the drop decelerates with respect to the ambient flow. It should be noted that as the drop decelerates, it also simultaneously deforms causing an increase in its frontal area, which can in turn increase surface shear stresses, given the velocity deficit is still substantial.

Most applications such as the internal combustion engine, spray painting, etc., involve a secondary fragmentation due to impulsive acceleration. Among impulsive acceleration cases, there can be different experimental systems such as a drop introduced into a uniform cross-flow, or a drop exposed to a shockwave in a wind tunnel. The timescales of an impulsive drop breakup process is relatively small, resulting in both the aforementioned experimental setup predicting similar critical Weber number for secondary fragmentation (Hsiang & Faeth 1992, 1995). Most of the experimental studies conducted on secondary fragmentation (Pruppacher & Beard 1970; Krzeczowski 1980; Wierzba 1990; Hsiang & Faeth 1992; Gelfand 1996; Theofanous *et al.* 2004; Szakáll *et al.* 2009; Jain *et al.* 2015; Kulkarni & Sojka 2014) have focused on impulsive acceleration, and those results are summarized in Figure 1.

After starting from an initial spherical shape, drops start the deformation process with flattening of the downstream face under the influence of pressure forces (Villermaux & Bossa 2009; Jain *et al.* 2019; Jackiw & Ashgriz 2021). This is followed by the formation of a pancake of one of the following two types: **(a)** a flat disk-like structure with both upstream and downstream faces showing an increase in radius of curvatures (henceforth called “flat pancake”); or **(b)** a pancake with a concave-shaped downstream surface, corresponding with minimal change in curvature of the upstream surface (henceforth called “forward pancake”) (Han & Tryggvason 2001). These differences in pancake shapes have been observed for differences in physical and flow parameters such as density-ratio  $\rho$ , initial Reynolds number  $Re_0$  (or outside Ohnesorge number  $Oh_o$ ) and drop Ohnesorge number  $Oh_d$ . However, the exact physical mechanism that causes this difference in pancake morphology has not yet been explored in the literature. Beyond the formation of a pancake, the pancake deforms further and starts to form a toroidal periphery (rim), which then leads to further deformation and possibly even breakup through different morphologies (discussed in the next paragraph). This stage, which marks the completion of pancake formation and the start of a visible peripheral rim, can be temporally indicated by a non-dimensional time  $t^* = t/\tau \approx 1$ . Here,  $\tau = D\sqrt{\rho}/V_0$  is the drop deformation timescale (Rimbert *et al.* 2020), where  $V_0$  is the uniform initial velocity of the ambient medium relative to the drop,  $D$  is the drop’s volume-averaged diameter, and  $t$  represents the elapsed dimensional time during the deformation process. This timescale is the same as the dimensionless time for Rayleigh-Taylor or Kelvin-Helmholtz instabilities specified by Pilch & Erdman (Pilch & Erdman 1987).  $\tau$  includes the effect of  $\rho$ , thus making  $t^*$  a useful temporal scale when comparing cases with different density-ratios.

Following the formation of a pancake after  $t^* > 1$ , the drop may further deform and ultimately breakup through one the the following morphologies (as illustrated in figure 1(a) to (e)): **(a)** Vibrational mode where the drop oscillates about a maximum deformation state, and does not show consistent breakup (Hsiang & Faeth 1992; Rimbert *et al.* 2020); **(b)** Simple Bag Breakup which involves the formation of a toroidal rim and

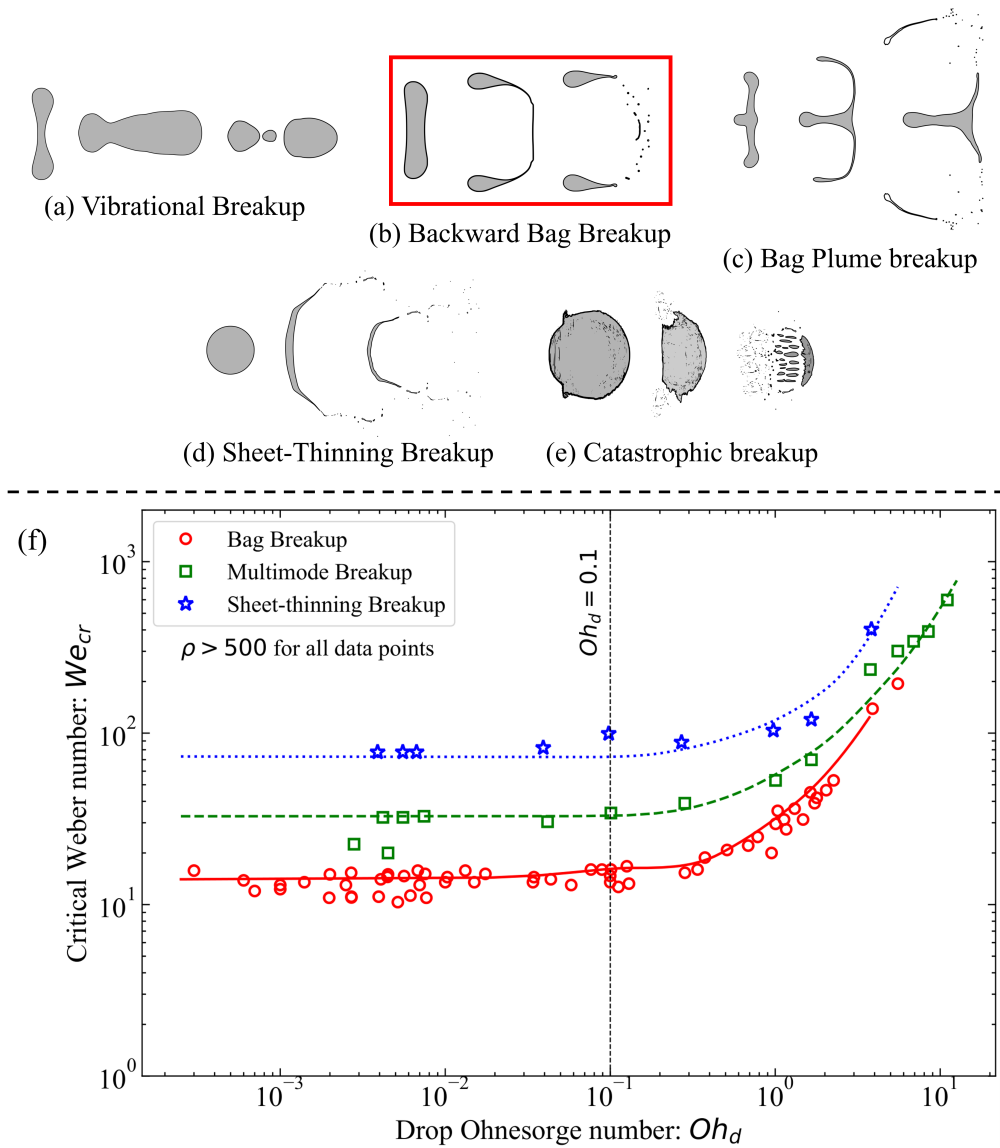


FIGURE 1. Types of drop breakup morphologies (Guildenbecher *et al.* 2009; Theofanous 2011) observed in experiments in order of increasing threshold Weber numbers are illustrated through figures (a) to (e). Figure (f) plots all the experimental data on threshold Weber numbers required to produce different fragmentation morphologies, based on a similar plot in Hsiang & Faeth (1995) and data from Krzeczkowski (1980); Pilch & Erdman (1987); Wierzbka (1990); Dai & Faeth (2001); Kulkarni & Sojka (2014); Jackiw & Ashgriz (2021); Han & Tryggvason (2001); Jain *et al.* (2019). Backward bag breakup, as shown in figure (b) in red box and the red curve in figure (f), has been the predominantly observed critical non-vibrational fragmentation morphology.

the inflation of a thin film (bag) in between, which ultimately ruptures due to Rayleigh-Plateau instabilities (Kulkarni & Sojka 2014; Jackiw & Ashgriz 2021); (c) a bag breakup with morphological features in addition to a bag, such as stamen/plume (Hsiang & Faeth 1995; Jain *et al.* 2015) or multiple bags (Cao *et al.* 2007; Jackiw & Ashgriz 2021); (d) Sheet Thinning breakup where thin sheets and ligaments are removed from the periphery

of the pancake, and are blown downstream relative to the drop core due to their low local inertia, ultimately breaking up due to instabilities (Khosla & Smith 2006; Gueldenbecher *et al.* 2009); and (e) catastrophic breakup where unstably growing surface waves pierce through the entire pancake and cause it to catastrophically disintegrate (Theofanous 2011).

In nature, under standard atmospheric conditions, most liquid-air drop-ambient systems have  $\rho > 500$ ,  $Oh_d > 0.001$ , and  $0.001 < Oh_o < 0.01$ . For this limited parameter space, most experimentally observed critical drop breakup morphologies have been simple bag breakups. On the other hand, most Direct Numerical Simulations (Han & Tryggvason 2001; Jalaal & Mehrovaran 2014) until the recent advent of Petascale computing have covered low density-ratios ( $\rho < 50$ ) due to computational limitations and lack of efficient adaptive mesh refinement algorithms. These simulations show a very different breakup process (e.g., forward pancake and bag formation) and critical Weber number values compared to the experiments. This hints at the vital role density-ratio plays in deciding drop breakup threshold and specific breakup morphologies. Only recently, DNS of drops with large density-ratios have become more common (Jain *et al.* 2015, 2019; Marcotte & Zaleski 2019; Dorschner *et al.* 2020) and further emphasizes the influence of  $\rho$  on the fragmentation threshold  $We_{cr}$ , as well as the threshold for the transition from bursting to stripping (Marcotte & Zaleski 2019). Jain *et al.* (2019) explored the effect of  $\rho$  on drop deformation for a specific  $Re_0$  and viscosity ratio for a range of  $We_0$  from 20 to 100, and observed the immense impact  $\rho$  has on the orientation of bags and pancakes, the drop velocities, and the total observed deformations. Similar conclusions were reached by Marcotte & Zaleski (2019) in relation to the effect of density-ratio on deformation morphology, with large  $\rho$  cases showing a higher incidence of plume (stamen) formation at the upstream pole of the drop.

By the 1990s, several experimental and theoretical works (Karam & Bellinger 1968; Krzeczowski 1980; Pilch & Erdman 1987) had established the important role of  $Oh_d$  in affecting the magnitude of  $We_{cr}$  for a drop-ambient system. This understanding was greatly expanded upon by Hsiang & Faeth's review paper in 1995 (Hsiang & Faeth 1995), where they aggregated all available experimental data from existing works as well as their own experiments, into  $We_{cr}$  vs.  $Oh_d$  plots. Their findings showed that the threshold  $We_0$  for the onset of all types of breakup morphologies (i.e., simple backward bag as well as other higher  $We_0$  breakup morphologies) follows a similar trend with respect to  $Oh_d$  (see figure 1 of Hsiang & Faeth (1995) or figure 1(f)), with the threshold  $We_0$  almost independent with respect to  $Oh_d$  for  $Oh_d < 0.1$ , and then increasing rapidly for  $Oh_d > 0.1$ . Furthermore, the critical breakup morphology (for the onset of breakup) for all the explored works were found to be simple bag breakups. It is essential to note that all the findings presented in Hsiang & Faeth (1995) were obtained for the parameter space previously specified to be experimentally feasible. Villermaux & Bossa (2009) was the first to analytically describe the bag breakup process for an inviscid drop and derived a constant threshold value of 6 for  $We_{cr}$ , an underestimation compared to experimentally seen threshold values. Their work was extended to include the viscosity of the drop fluid, first by Kulkarni & Sojka (2014) and most recently by Jackiw & Ashgriz (2021), resulting in a function of  $Oh_d$  that describes  $We_{cr}$ . This corrected for the underestimation and led to a great match with previous experimental results. The analytical works mentioned above do not take into account ambient fluid properties such as ambient viscosity ( $Oh_o$ ) and density ( $\rho$ ) (which in turn dictates the relative velocity of the drop with the ambient) in influencing the resulting deformation characteristics. However, the density and viscosity contrasts between the ambient and drop fluids are generally very large for experimental systems, thus minimizing the significance of ambient fluid properties

relative to that of the drop. This allows for a good match between the analytical solution and corresponding experimental  $We_{cr}$  values, even with the aforementioned assumptions. However (as will be explored in detail in this work), for systems where the contrast between the (physical properties of) ambient and drop fluids is not substantial, these factors must be taken into account for the correct estimation of threshold  $We_0$  values.

The (almost) independence of drop fragmentation threshold with respect to  $Oh_d$  for  $Oh_d < 0.1$  as observed in most experimental works has an interesting side-effect — it has become a common practice to assume a constant arbitrary  $Oh_d$  value of less than 0.1 for most analysis as a representative value for all low viscosity drop breakups. Very few works have exhaustively explored the effect of varying  $Oh_d$  for  $Oh_d < 0.1$ . One such work is that of [Jain \*et al.\* \(2019\)](#) where they explored the effect of viscosity ratio (and hence  $Oh_d$ ) on breakup morphologies through simulations of drops of  $\rho = 1000$  and two different viscosity ratios, and observed that the threshold values of  $We_0$  decreased with decreasing  $Oh_d$ . They also observed the appearance of a plume at the upstream pole for lower viscosity ratio cases for the same  $We_0$ .

Initial Reynolds number  $Re_0$  (or alternatively Ambient Ohnesorge Number  $Oh_o$ ) also remains to be exhaustively explored, especially in the context of critical drop breakup threshold. [Han & Tryggvason \(2001\)](#) did simulations for different  $Re_0$  values for some low density-ratio cases, and observed large reduction in drop deformations for low  $Re_0$  values. They speculated that this reduction in deformation might lead to an increase in  $We_{cr}$  values. Very few other works have explored or commented on the role of  $Oh_o$  on drop breakup ([Guildenbecher \*et al.\* 2009](#); [Jain \*et al.\* 2019](#); [Marcotte & Zaleski 2019](#)). [Jain \*et al.\* \(2019\)](#) once again was one of the very few works to analyze the impact of  $Re_0$  on high density-ratio drops ( $\rho = 1000$ ) and observed higher incidences of plume formation in backward bag morphology for higher  $Re_0$  values.

Hence, there is the need for a single cohesive study analyzing the effect of all the relevant non-dimensional parameters,  $Oh_o$ ,  $Oh_d$ , and  $\rho$  on drop deformation and breakup, and their impact on the threshold Weber number observed for critical breakup ( $We_{cr}$ ). In this study we quantify the effect of each of these parameters using high-fidelity multiphase flow simulations. It should be noted that a distinction between liquid-gas and liquid-liquid drop-ambient systems has been maintained in the existing literature. However, fundamentally, the only differentiating factor between the two systems is the density and viscosity ratios, as well as the surface tension of the fluid interface. It is expected that the need for this distinction should vanish for a study that covers a sufficiently large parameter sweep involving  $\rho$ ,  $Oh_o$  and  $Oh_d$ . Thus, a wide range of values of  $\rho$  and  $Oh_o$  have been quantified.  $Oh_d$  values explored in this study are restricted to  $Oh_d \leq 0.1$ , to focus at a range rarely explored in existing studies.

The paper starts with a description of the relevant impulsive acceleration problem (section 2.1), the high-fidelity numerical model (section 2.2 and 2.3). The parameter space to be numerically explored is described in detail in section 2.4. The effects of  $Oh_d$ ,  $Oh_o$ , and  $\rho$  on the drop deformation, given that other parameters are constant, are described in detail, illustrating the forces and internal flow observed in the drops (section 3). During the course of the parameter sweep, by simulating a range of Weber number values for every non-dimensional parameter set, the corresponding critical Weber number can be discovered. Based on the insights gained from the simulations, a novel non-dimensional parameter ( $C_{breakup}$ ) has been derived, incorporating the effects of all the relevant non-dimensional numbers.  $C_{breakup}$  is found to be more effective in predicting the threshold of drop fragmentation, over the currently used  $We_{cr}$ .

## 2. Problem Description and formulation

### 2.1. Problem Description and Non-dimensionalisation

Let us consider a drop of diameter  $D$  containing a fluid of density  $\rho_d$  and dynamic viscosity  $\mu_d$  (subscript  $d$  implies properties associated with the drop). It is impulsively accelerated by a uniform flow of velocity  $V_0$ , of density  $\rho_o$  and viscosity  $\mu_o$  (subscript  $o$  implies properties associated with the ambient medium, i.e., outside the drop), starting at  $t = 0$ . The surface tension of the drop-ambient interface is  $\sigma$ .

Based on these initial conditions, we can define an initial Weber number  $We_0$  ( $\rho_o V_0^2 D / \sigma$ ).  $We_0$  represents the competition between the dynamic pressure forces that drive the deformation of the drop and the capillary forces that resist this deformation. An increase in  $We_0$  corresponds to an increase in the maximum deformation achieved by the drop before it retracts to its equilibrium shape of a sphere, due to the action of surface tension. We then expect there to be a maximum  $We_0$  for which the surface tension forces barely prevent fragmentation in the drop. This threshold is called the critical Weber number  $We_{cr}$  ( $\rho_o V_{cr}^2 D / \sigma$ ), where  $V_{cr}$  corresponds to the critical (lowest possible)  $V_0$  required to consistently realize a non-vibrational breakup.

Subsequently, a Buckingham-Pi analysis for this system reveals all the non-dimensional parameters on which  $We_{cr}$  most generally depends upon (equation (2.1)).

$$We_{cr} = F(\rho, Oh_o, Oh_d) \quad (2.1)$$

The density-ratio  $\rho$  ( $\rho_d / \rho_o$ ) is a measure of the inertia of the drop relative to the ambient medium, reflecting its responsiveness to external forces. The dynamic pressure forces exerted by the ambient medium scale with  $\rho_o$ , i.e., its effectiveness in inducing accelerations in specific parts (such as the peripheral rim or the core) or in the entirety of the drop is inversely proportional to  $\rho$ .

The drop Ohnesorge number  $Oh_d$  ( $\mu_d / \sqrt{\rho_d \sigma D}$ ) is a ratio of capillary and momentum diffusion time scales and provides an estimate of how the energy supplied to a drop by external forcing is distributed among surface energy and viscous dissipation.

The ambient Ohnesorge number  $Oh_o$  ( $\mu_o / \sqrt{\rho_o \sigma D}$ ) provides a non-dimensional, velocity-independent analogue for the initial Reynolds number  $Re_0$  (since  $Oh_o = \sqrt{We_0} / Re_0$ ), and represents ambient viscosity given that other parameters are the same.

Across the timescales over which a drop deforms and fragments, it can undergo significant centroid accelerations and also deform significantly. This necessitates consideration of an instantaneous Reynolds number  $Re$  ( $\rho_0 V_{rel} D_{rel} / \mu_o$ ) in addition to  $Re_0$ , based on the drop's instantaneous velocity deficit ( $V_{rel}$ ) with the ambient medium and its frontal radius for the instantaneous deformed shape ( $D_{rel}$ ).

If we choose  $\rho_o$ ,  $V_0$  and  $D$  as the basis variables for non-dimensionalising the system, the dimensional variables can be non-dimensionalized as follows:  $\hat{\rho}_d = \rho$ ,  $\hat{\sigma} = 1 / We_0$ ,  $\hat{\mu}_o = Oh_o / \sqrt{We_0}$ , and  $\hat{\mu}_d = Oh_d \sqrt{\rho} / We_0$ .

Hence, for a specific ambient-drop fluid combination (i.e. fixed physical properties), a specific drop diameter, and a specific inflow velocity, a set of  $\{\rho, Oh_o, Oh_d, We_0\}$  can be obtained that fully characterizes the system. A drop can be simulated in Basilisk to assess whether it undergoes a non-vibrational breakup for the corresponding non-dimensional set. If the drop does not fragment,  $We_0$  is systematically increased (attributable to a decrease in  $\sigma$  in non-dimensional space, or an increase in inflow velocity in dimensional space) and the impulsive acceleration simulation is rerun. These steps are repeated until the drop exhibits a non-vibrational breakup. The corresponding minimum  $We_0$  that marks the onset of non-vibrational breakup is the critical Weber number  $We_{cr}$  for that particular non-dimensional set  $\{\rho, Oh_o, Oh_d, We_0\}$ .

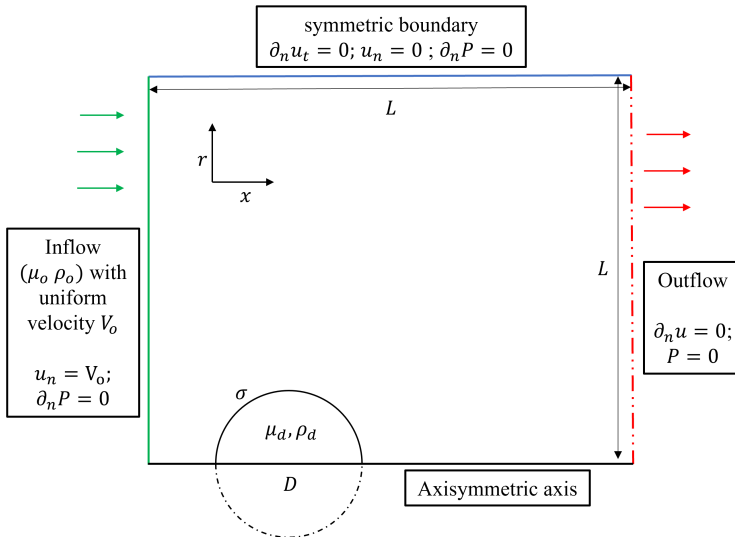


FIGURE 2. The axisymmetric domain used for all simulations in this work; At  $t = 0$ , the simulation starts with a stationary axisymmetric spherical drop under impulsive acceleration.

## 2.2. Model Description

The simulations were conducted employing the open-source solver suite "Basilisk" ([www.basilisk.fr](http://www.basilisk.fr)), a set of open-source codes designed to address a variety of partial differential equations on adaptive Cartesian meshes. Basilisk (and its predecessor "Gerris") have undergone extensive validation across a range of fundamental problems associated with two-phase flows (Popinet 2003, 2009; Marcotte & Zaleski 2019). This extensive validation establishes Basilisk as the ideal solver to conduct drop simulations, over a wide range of  $\rho$  and  $\mu$  values. For this work, we utilized its Navier-Stokes centered solver in conjunction with its two-phase flow formulation to simulate the drops. A more detailed description of the numerical scheme relevant for this work is presented in appendix A, and in Popinet (2003, 2009). This section focuses solely on the assumptions and simulation parameters specific to the problem under consideration.

This work requires a large number of simulations to perform a complete parametric sweep across the parameters specified in equation 2.1(c). Consequently, 3D simulations become computationally infeasible. Moreover, the process of deformation of a drop under impulsive acceleration, particularly when close to or below critical conditions, is axisymmetric in nature for the majority of the process — from the initial pancake formation until the inflation of the pancake into a bag. It is the final inflation of the expanding bag and the corresponding rupture, driven by interfacial instabilities, that cannot be assumed to be axisymmetric. The primary focus of this work is to characterize the deformation morphologies exhibited by a drop throughout its deformation process and its ultimate fate — whether the drop breaks up, and its general fragmentation morphology if it does fragment. The precise details of the fragmentation morphology, such as bag size or the final drop size distribution after fragmentation, which would necessitate a fully resolved 3D DNS, are not critical to the objectives of this study. Therefore, for the purposes of this work, axisymmetric simulations suffice. The validity of this assumption of axisymmetry in the context of this work will be assessed in section 2.3.

The general simulation domain, used for the simulations in this study, is illustrated in

figure 2. It is a square (for compatibility with quadtree meshes) axisymmetric domain of size  $L$  and its dimensions are carefully chosen to ensure that the drop always remains a sufficient distance from the boundaries.  $L$  can be as small as 16 for drops with high inertia ( $\rho \geq 100$ ), and as large as 64 for drops with low inertia ( $\rho = 10$ ). The top boundary is symmetric ( $\partial_n P = \partial_n u_t = u_n = 0$ ) and the bottom boundary is the axisymmetry axis. The left boundary allows a uniform ambient fluid inflow into the domain ( $u_n = V_0 = 1$ ), and the right boundary allows the flow to exit the domain freely ( $\partial_n u_n = 0$ ). A drop of diameter  $D = 1$  is initialized with its center on the axisymmetric axis and its initial velocity set to 0.

To ensure sufficient solution accuracy, we enforce the maximum allowed wavelet errors to  $u_e = 10^{-4}$  and  $c_e = 10^{-6}$  for velocity and volume fraction fields, respectively. The maximum allowed refinement level is set to 512 cells per diameter ( $N = 13$  for  $L = 16$ ) for all cases except for cases with  $Oh_o = 0.0001$  which correspond to the highest values of  $Re_0$ , for which we use 1024 cells per diameter ( $N = 14$  for  $L = 16$ ). Grid independence tests, detailed in appendix B, guide the choice of error thresholds and refinement levels used for all production runs in this study.

A significant fraction of the simulations in this study involve high density-ratios ( $\rho > 500$ ). For such high density-ratios, a sharp interface can induce instabilities at the interface due to an unnatural spike in kinetic energy (Jain *et al.* 2015). The phenomenon has also been observed in all of our large  $\rho$  simulations with low  $Oh_d$  ( $Oh_d \leq 0.001$ ), albeit not presented here. In these cases, the upstream face shows unnaturally large surface instabilities, which lead to the removal of micro-droplets from the main drop. To overcome these issues, we smear the interface vertex averaging the volume fraction field  $c$ . This approach helps to reduce density gradients across the interface, preventing its premature breakup. The numerical scheme with this smearing will be validated for a high  $\rho$  case in the next section.

At  $t=0$ , the ambient fluid is quiescent and the drop is initialized with zero initial velocity. Given the incompressible nature of the flow and an infinite propagation speed of any information across the domain, the end of the 1<sup>st</sup> timestep sees the entire domain attain a flow consistent with the left inflow boundary conditions. This involves the establishment of an incompressible flow around the drop, requiring the velocity field to be solenoidal. In real life, this process occurs in a finite amount of time, dependent on the velocity of the acoustic wave velocity. However in a numerical system, this occurs in a single timestep and leads to a jump in drop centroid velocity, without gaining any corresponding deformation. The magnitude of this velocity jump in its centroid velocity  $\delta V$  is inversely proportional to  $\rho$  (Marcotte & Zaleski 2019). Hence, the effective relative velocity at undeformed state of the drop reduces to  $V_{eff} = 1 - \delta V$ . Accounting for this effective velocity becomes imperative when calculating the associated  $We_0$  of the system. To address this, simulations have been conducted for each pertinent  $\rho-Oh_o$  pair, resulting in the following observed velocity jumps — a substantial jump of approximately 0.14 for  $\rho = 10$ , a jump of 0.030 for  $\rho = 50$ , and a negligible velocity jump of 0.015 ( $\sim 1.5\%$ ) for  $\rho = 100$ . For all simulations with  $\rho > 100$ , this 1<sup>st</sup> timestep jump is deemed insignificant. All non-dimensional parameters in the current work have been corrected to incorporate this jump.

### 2.3. Verification of Axisymmetric drop Simulations

To verify the capabilities of Basilisk in modeling high density-ratio drops subjected to impulsive acceleration, we reproduce the Bag breakup experiment as described in Flock *et al.* (2012). An ethyl alcohol drop is released from a certain height above an approximately uniform jet of air. The drop undergoes a nearly quiescent free-fall for a



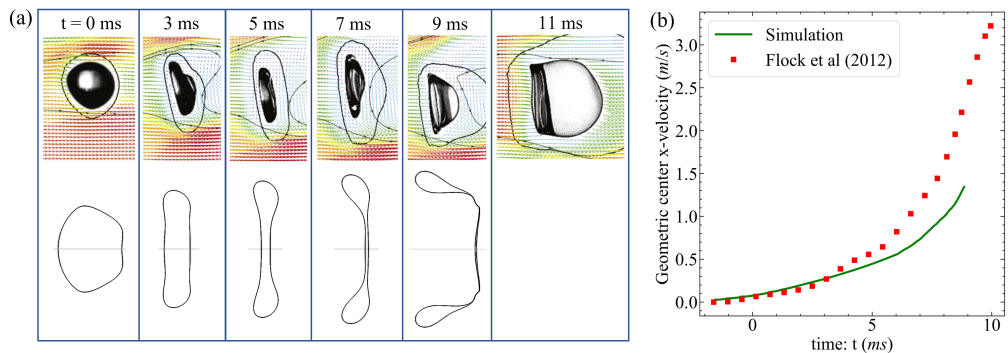


FIGURE 3. (a) compares drop deformation with time for Flock *et al.* (2012) (top) and analogous Basilisk Simulation (bottom). (b) compares geometric-center based x-velocity for Bag breakup case from Flock *et al.* (2012) to corresponding Basilisk simulations.

height of 188 mm before entering a jet of air of mean velocity of 10 m/s and a peak velocity of 15 m/s. The drop, having acquired some vertical velocity during its fall, has a shape that is close to but not perfectly spherical when it enters the air-jet. The drop then deforms as a result of aerodynamic forces exerted by the air-jet and finally breaks up according to a bag breakup morphology. As the drop enters the jet, it initially experiences aerodynamic forces applied by the boundary layer of the flow, and then moves into the main flow with peak flow velocities.

A simplified axisymmetric version of this experiment is simulated in Basilisk with non-dimensional parameters derived from the dimensional parameters specified in Flock *et al.* (2012). The simulation parameters are  $V = 1$ ,  $Oh_o = 2.3 \times 10^{-3}$ ,  $Oh_d = 5.9652 \times 10^{-3}$ , choice of  $We_0$  depends on the choice of air-jet velocity between 10 and 15 m/s,  $L = 16$ , and  $D = 1$ . The simulation differs from the experiment in multiple, although minor ways. Firstly, the initial free fall of the drop is omitted since a gravity force perpendicular to the jet direction would render the system non-axisymmetric. Consequently, the slight deformation of the drop just before encountering the air-jet is captured in the simulation. Secondly, unlike the experiments where the drop passes through a boundary layer of thickness approximately 3 mm before experiencing the peak 15 m/s jet velocity, the simulations instantaneously load the drop with the full velocity of the air-jet. Considering that the provided  $We_0 = 13$  is based on the mean jet velocity, it will be essential to find the  $We_0$  appropriate for our simulation conditions (instantaneous loading), corresponding to velocities between 10 and 15 m/s.

It is important to note that the drop velocities reported in Flock *et al.* (2012) are computed through a central difference of the geometric-center of the shadow of the drop, i.e. outer contour of the drop as seen from the side, with respect to time. Since the bag in a bag breakup contains a very small fraction of the total drop volume, a geometric-center does not match with volume averaged center of the drop fluid once the bag has sufficiently inflated. Hence, we obtain geometric-center based drop velocity from the simulation and use it for comparison.

The comparison between drop deformation morphology and geometric-center x-velocity for both experiment and simulation is plotted in figure 3. (a) compares experimental drop morphology to the corresponding axisymmetric Basilisk simulation. It is observed that the simulations effectively capture the deformation characteristics until time  $t = 7$  ms, including the shape of the pancake and the magnitude of the deformation. This is also corroborated by the velocity plot shown in (b), where the x-

---

Parameters	Values	Computational cells
$\rho$	10, 50, 100, 500, 1000	
$Oh_o$	0.1, 0.01, 0.001, 0.0001	Min: $1.75 \times 10^5$
$Oh_d$	0.1, 0.01, 0.001	Max: $4 \times 10^6$

---

TABLE 1. All values of  $\rho$ ,  $Oh_o$ , and  $Oh_d$  which form the part of the parametric space to be explored through simulations are listed in this table. In total, 60 sets of  $\{\rho, Oh_o, Oh_d\}$  are considered, each is simulated for multiple  $We_0$  values to obtain its  $We_{cr}$ . The minimum and maximum number of cells in the computational domain associated with all simulations is listed in the third column.

---

velocities for the experiment and the simulation closely match until approximately  $t = 6$  ms. However, as the drop deformation reaches the bag inflation stage, the axisymmetric simulations and the experiments start to diverge. Although the general morphology of breakup (i.e. bag breakup) is replicated by the simulations, there is a discernible discrepancy between the exact size of the bag and the corresponding toroidal rim. Since the drop centroid acceleration is directly proportional to its frontal area, a smaller bag size in the simulations results in smaller accelerations.

This divergence observed between the simulations and the experimental results, especially in later stages, when the drop is in bag inflation stage, can be attributed to the differences between the idealized simulation setup and the experiment, as noted previously in detail. Notable differences include the presence of acceleration due to gravity in the experimental setup and differences in initial conditions (initial deformation and velocity) of the drop. The experiments inherently lack axisymmetry and can only be approximately replicated by an axisymmetric simulation under the condition that the timescales involved in the impulsive breakup process is much smaller than the timescales associated with gravity-driven drop deformation. Furthermore, the ultimate bag rupture process has been canonically attributed to instabilities (Lozano *et al.* 1998; Bremond & Villermaux 2005; Villermaux 2007; Zhao *et al.* 2011), which are inherently three-dimensional in nature. However, for the objectives of this study, accurate information on the exact size of the bag, its rupture location, or the resulting drop size distribution is not essential.

Accurate information pertaining to the initial deformation morphology of the drop (such as the pancake shape), and its corresponding general breakup morphology (such as bag, bag-plume, sheet-thinning, etc.) is sufficient to conduct a broad categorical analysis on the sensitivity of these features to parameters such as  $Oh_o$ ,  $Oh_d$  and  $\rho$ . This information can be reliably obtained through axisymmetric simulations.

Finally, we conduct 3D and axisymmetric simulations for drop-ambient systems with low density-ratios and ambient Ohnesorge numbers. Both 3D and axisymmetric cases show extremely similar aspect ratios and x-velocities for the majority of the deformation process, and further justify the use of axisymmetric simulations in this study. A detailed description of this comparison is presented in appendix C.

#### 2.4. Parameter space explored

The goal of this work is to systematically study the influence of the three non-dimensional parameters discussed, namely  $\rho$ ,  $Oh_o$ , and  $Oh_d$ , on drop deformation and breakup morphology. Table 1 summarizes the parameter space explored through simulations in this work, encompassing 60 sets of  $\{\rho, Oh_o, Oh_d\}$ . Each set is simulated for differ-

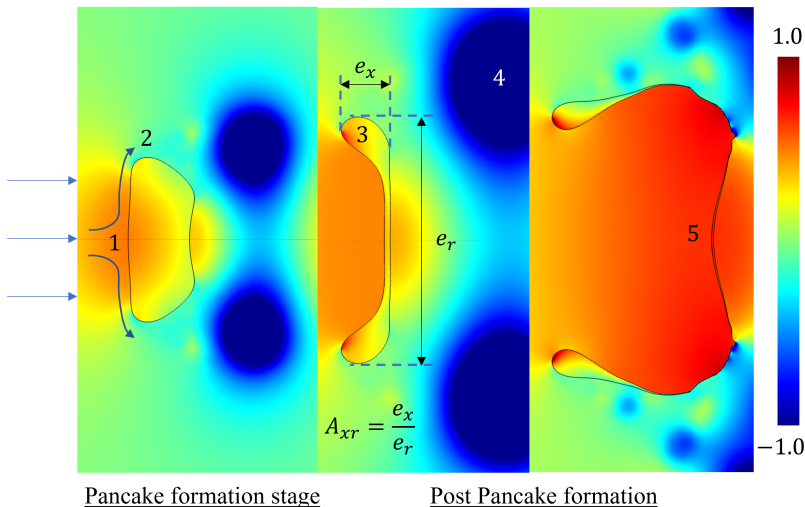


FIGURE 4. The figure shows the points of interest in a deforming drop. 1. Upstream pole / Center / Core of the drop; 2. The periphery of the drop; 3. The rim of the drop, which in general has a higher local inertia compared to its center; 4. Downstream low pressure circulation zone, which can affect the motion of its rim if it is attached to the drop surface (unlike in the figure); 5. The inflated bag, which inflates because of its low inertia and hence higher accelerations.

ent  $We_0$  values in order to identify its critical Weber number  $We_{cr}$  and the corresponding critical breakup morphology. This is achieved by simulating each  $\{\rho, Oh_o, Oh_d\}$  set with multiple  $We_0$  values to determine the lowest  $We_0$  value at which a non-vibrational breakup is observed, in short its  $We_{cr}$ .

Given  $Re_0 \propto 1/Oh_o$ , a range of  $Re_0$  in the order of  $(10, 10^4)$  corresponds to a  $Oh_o$  range of  $(0.0001, 0.1)$ . Any higher  $Re_0$  becomes computationally infeasible due to significant turbulent vortices in the domain leading to a requirement for higher mesh resolution, lower timestep sizes, and even 3D simulations. Hence, this justifies the parameter space specified for  $Oh_o$ .

The impact of  $Oh_d$  on  $We_{cr}$  has been explored in existing literature for large  $\rho$  and  $Oh_o$  values, commonly seen in experimental systems. However, the same cannot be said for low  $\rho$  or extreme (very small or large)  $Oh_o$  values, where influence of  $Oh_d$  remains unexplored. In fact in many studies,  $We_{cr}$  is often assumed to be constant for all cases with  $Oh_d < 0.1$ , irrespective of the values of  $\rho$  and  $Oh_o$ . Through this work, we aim to scrutinize the validity of such assumptions when  $\rho$  and  $Oh_o$  vary in the chosen parameter space, thus justifying our decision to vary  $Oh_d$  in the range  $(0.1, 0.001)$ .

Finally, to encompass the entire spectrum of low and high density-ratio systems,  $\rho$  values are systematically varied from 10 to 1000.

The choice of such a comprehensive parameter exploration sets the stage for a detailed investigation into the nuanced interplay of these parameters on drop deformation and breakup characteristics.

### 3. Results

Illustrated in figure 4 is an example of drop deformation that starts with the formation of a flat pancake and eventually breaks up with a backward bag morphology. The figure specifies (as numbered markers) the important locations and features during

drop deformation, serving as a reference for the definition of the factors essential in understanding a drop's deformation. They are as follows:

1. The local variation in inertia across the drop, which determines the local accelerations of the constituent parts, e.g., the difference in local inertia between the center (1) and rim (3).

2. The pressure difference between the poles (1) and periphery (2), denoted by  $\Delta P_{drive}$ .  $\Delta P_{drive}$  is directly proportional to the stagnation pressures observed at the upstream pole of the drop.

3. The surface stresses or viscous forces experienced by the drop surface, especially its upstream facing surface. Viscous stresses are a function of the instantaneous Reynolds number  $Re$  around the drop. Given that  $Re_0$  for most situations dictates the order of magnitude of  $Re$ ,  $Re$  can be approximated as equal to  $Re_0$  if the evolution with time of centroid velocities and drop deformation do not significantly alter  $Re$ .

4. The drop Ohnesorge number  $Oh_d$ , which dictates the distribution of the total energy supplied by the ambient flow to the drop between surface energy and the fluid momentum gained by the drop.

Together, these factors provide an intuitive framework for understanding the intricate dynamics of drop deformation and breakup, and will be referred to for all such discussions in this study.

From the start of the deformation process until the formation of a distinct rim at  $t^* \approx 1$ , a drop does not exhibit any appreciable variation in local inertia along the lateral dimension. Hence, during this initial deformation phase, local inertia differences do not significantly influence the initial deformation; instead, the interplay between pressure and shear forces predominantly governs the process. Centroid acceleration and hence centroid velocity is inversely proportional to total inertia and directly affects instantaneous Reynolds number  $Re$  of the ambient flow past the drop. While  $Re$  dictates the shear stresses on the upstream surface, the relative velocity of the drop dictates the stagnation pressures at the upstream pole and hence  $\Delta P_{drive}$ . The resulting pancake shape depends on the comparative strengths of the pressure difference and shear forces.

Once a drop develops local inertia variations across the lateral dimension as it deforms past the pancake stage, any subsequent deformation becomes strongly dependent on these variations in local accelerations. For the same external forces, regions of the drop with larger inertia experience much lower accelerations, and hence lag behind their lower inertia counterparts.

$Re$  of the ambient flow past the drop dictates the strength, timescales, lengthscales, and location of the downstream vortices (Forouzi Feshalami *et al.* 2022). Thus, it is essential that we consider the interaction of these vortices with the rim for different  $Re$  values to understand the final shape. The sensitivity of the rim to these flow characteristics is decided almost solely by inertia relative to the ambient fluid, i.e.,  $\rho$ . A large density-ratio drop is expected to exhibit very little sensitivity to downstream vortices, and conversely, a low density-ratio drop is expected to be more responsive to such vortical structures.

If we consider the specific drop case shown in figure 4, the ratio of spatial extent of the drop along the axisymmetric axis to the spatial extent along the  $r$ -axis provides its aspect ratio  $A_{xr}$ . This parameter will be used in future sections to quantify the deformation shown by the drops for the parameter space. In the first image (from left to right), we observe a flat pancake, which occurs when  $\Delta P_{drive}$  predominantly drives the internal flow in the drop (over shear stresses). We also observe a clear toroidal rim (image 2) that has a large local inertia and is therefore expected to lag the lower inertia center of the drop. Due to the large inertia, the rim remains unaffected by the low-pressure zone created by the downstream vortex, which sheds a sufficient distance away from the

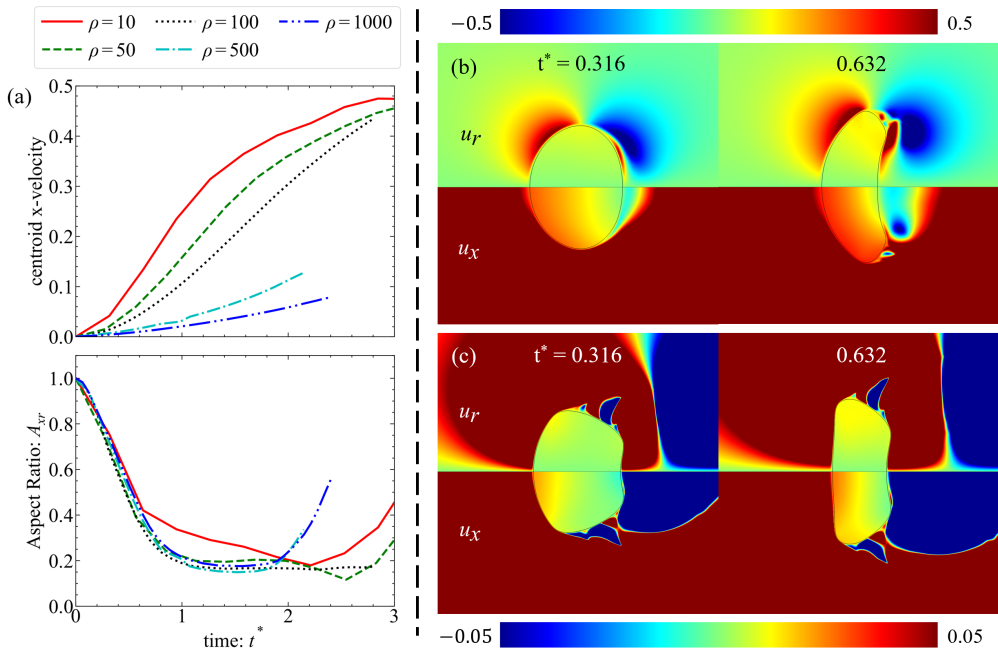


FIGURE 5. (a) shows the temporal variation of centroid x-velocity and Aspect Ratio of drops with different  $\rho$  values. Internal velocity fields are plotted for (b)  $\rho = 10$  and (c)  $\rho = 1000$ . The upper half shows r-velocities, whereas the lower half of each plot shows x-velocities. All drops referred here have  $Oh_o = 0.001$ ,  $Oh_d = 0.1$ ,  $We_0 = 20$ .

rim and is not attached to the drop. Ultimately, the drop deforms into a backward bag morphology, where the center inflates into a bag under the action of pressure forces at the stagnation point.

### 3.1. Density-ratio

This section illustrates the role of density-ratio in influencing drop deformation and breakup morphology. Figure 5(a) illustrates the variation of drop centroid velocity and aspect ratio ( $A_{xy}$ ) (defined in figure 4) over time for density-ratios from 10 to 1000. The centroid velocity plot shows the direct influence of total inertia of the drop on its centroid acceleration. The lowest  $\rho$  drops experience the highest centroid accelerations and hence tend to achieve the free-stream velocity the quickest. This results in lower stagnation pressures at the upstream poles and lower values of  $Re$  for low  $\rho$  drops. Alternatively, one can interpret this as the sensitivity of the drop to external forces — a drop with a large  $\rho$  exhibits smaller local accelerations compared to low  $\rho$  drops under the same forces within the same time interval. Therefore, the responsiveness of a drop to downstream vortices directly depends on  $\rho$ .

The temporal development of the aspect ratio for different values of  $\rho$  is also shown in figure 5(a). Up to the completion of pancake formation at  $t^* \approx 1$ , all drops show a decrease in  $A_{xy}$  over time. This initial stage, which spans  $0 < t^* < 1$ , corresponds to the longitudinal flattening of the drop from a sphere to a pancake. At  $t^* \approx 1$ , the drop achieves its lowest aspect ratio as a pancake. Any subsequent deformation past the pancake stage leads to the formation of a distinct and prominent rim, signifying the end of this stage.

Let us start our exploration of the influence of density-ratio on drop-ambient systems

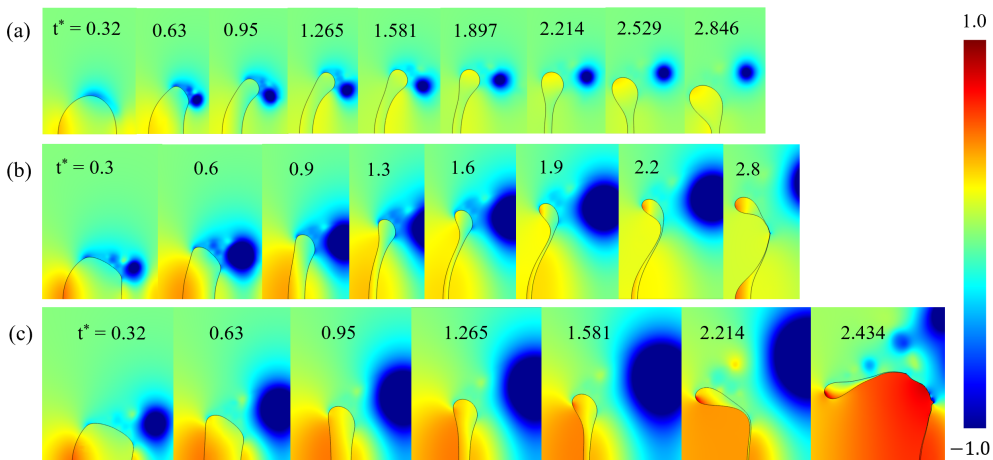


FIGURE 6. Pressure field plots for drops with three different density-ratios are plotted (a)  $\rho = 10$  (b)  $\rho = 100$  (c)  $\rho = 1000$  for a low  $Oh_o$  system. All drops referred here have the following common parameters:  $Oh_o = 0.001$ ,  $Oh_d = 0.1$ ,  $We_o = 20$ .

characterized by a low ambient Ohnesorge number  $Oh_o$ . The plots relevant to these cases are presented in figure 5(b), (c) and 6. The common  $Oh_o$  chosen for these cases is  $Oh_o = 0.001$ , corresponding to  $Re_o \approx 4472$ . This high  $Re_o$  results in lower shear stresses acting on the drop's upstream surface, compared to a case with high  $Oh_o$  (such as  $Oh_o = 0.1$  in figure 7).

Until the formation of a distinct toroidal rim at  $t \approx 1$ , local inertia variations across the lateral dimension of a drop remain small and therefore do not significantly influence the corresponding local accelerations experienced by each region of the drop. Hence, during the pancake formation stage, the deformation is primarily dependent on the balance between the shear and pressure forces applied by the ambient medium.

A low  $\rho$  drop has lower relative velocities with the free-stream compared to a large  $\rho$  case, resulting in a lower pressure difference between the upstream pole and periphery ( $\Delta P_{drive}$ ). This is illustrated by the pressure field plots in figure 6(a), where the lowest stagnation pressures are observed for the lowest density-ratio ( $\rho = 10$ ) case. A low  $\Delta P_{drive}$  allows even the low shear stresses applied by the low  $Oh_o$  (i.e., high  $Re_o$ ) ambient flow to dominate the deformation process. Hence, we expect the initial deformation and internal flow to be predominantly driven by shear stresses acting on the upstream surface of the drop. This is verified through the internal flow plots corresponding to figure 6(a) shown in figure 5(b). The internal flow is highest near the upstream surface and decreases to nearly zero at the downstream pole (see  $u_x$ ), with the corresponding velocity gradient pointing in a direction normal to the upstream surface. This flow profile indicates that the internal flow characteristics are dictated by shear stresses. We also observe that the internal velocities near the periphery of the drop are the largest, indicating that the periphery experiences the largest velocity gradient and consequently, the largest shear stresses. This, coupled with the lack of local inertia differences across the lateral dimension of the drop (before  $t^* \approx 1$ ), results in a larger downstream local acceleration at the periphery relative to the center, resulting in a forward-facing pancake. Furthermore, the lower relative velocity of the drop with the ambient leads to lower  $Re$  values, resulting in a weaker downstream circulation zone. Given the extremely low inertia, the drop rim is still influenced by the weak induced drag applied by this downstream vortex, contributing

to a forward pancake morphology. As a result, the vortex does not fully detach from the drop rim and sheds nearer to the periphery during the pancake formation stage.

This dominance of shear stresses over  $\Delta P_{drive}$  is less evident for an intermediate  $\rho$  drop such as the one illustrated in figure 6(b), where the stagnation pressures are higher than those in (a). This increased  $\Delta P_{drive}$  is large enough to match the contribution of shear stresses to its internal flow, resulting in a pancake that is somewhere between flat and forward facing.

For the drop with large  $\rho$  values, as shown in figure 6(c), the stagnation pressures are even higher, making  $\Delta P_{drive}$  the dominant factor over shear stresses in deciding its internal flow. This is apparent from internal flow fields as shown in figure 5(c), where the highest x-velocities are seen at the upstream pole, and not at the periphery, in contrast to the  $\rho = 10$  case (figure 5(b)).

As the drop deforms beyond the pancake stage (at  $t^* \approx 1$ ), the formation and growth of a prominent rim is observed in all three cases shown in figure 6. Once a major fraction of the drop fluid has been transferred to the rim, local inertia differences between the center and periphery start to influence the local accelerations across different regions of the drop. Moreover, the frontal radius increases as the drop deforms further towards a bag morphology. In certain instances, such as for  $\rho = 1000$ , this radial expansion can compensate for the reduction in relative velocity, leading to an increase in  $Re$  and the strengthening of low-pressure circulation zone downstream of the drop.

For a low  $\rho$  case such as figure 6(a), the downstream vortex shows minimal growth owing to a substantial centroid velocity and comparatively small radial expansion. By  $t^* = 1.581$ , the small induced drag on the drop rim has been overcome by the differences in local inertia between the center and periphery. The rim starts to decelerate relative to the center and flips from a forward to a backward bag morphology. By  $t^* = 1.897$ , the downstream vortex has fully developed and detached from the periphery, ceasing its influence on drop deformation. The low relative velocities with ambient (due to its low inertia) also result in lower overall aerodynamic forcing driving the drop deformation, leading to a bag morphology at  $t^* = 2.214$  without deforming enough to undergo fragmentation.

For a large  $\rho$  case such as figure 6(c), the high relative velocities with respect to the free-stream, coupled with the large radial growth, result in a stronger downstream circulation zone. However, the large inertia causes the drop rim to detach from the downstream vortex as early as  $t^* = 0.632$ , and hence experiences negligible local induced drag at the rim beyond this point. This, combined with the already dominant  $\Delta P_{drive}$ , leads to only lateral growth (flattening) of the pancake from  $t^* = 0.948$  to  $t^* = 1.581$ . As local inertia differences between the center and periphery become substantial, the rim starts to decelerate relative to the center and hence forms a backward bag. Figure 6(c) depicts this behavior from  $t^* = 1.581$  to  $t^* = 2.434$ .

For an intermediate  $\rho$  case such as the one presented in figure 6(b), the drop has a larger inertia compared to a lower  $\rho$  case, which leads to stronger downstream vortices, owing to a larger  $Re$ . Nevertheless, the local inertia of the rim is still not sufficient to detach the periphery from the developing downstream circulation zone, resulting in larger lateral stretching rates. For a low  $\rho$  case, the downstream vortices are never strong enough to generate sufficient lateral stretching, whereas for a high  $\rho$  case, the inertia differences are sufficiently large to allow the rim to detach from the circulation zone early. Only an intermediate  $\rho$  case allows large enough  $Re$  to generate a strong downstream vortex, and yet low enough inertia for the rim to be influenced. The evacuation rate of the drop core towards the periphery, driven by  $\Delta P_{drive}$  is still relatively small for intermediate drop inertia values. Consequently, the drop initiates the bag formation process, even when the

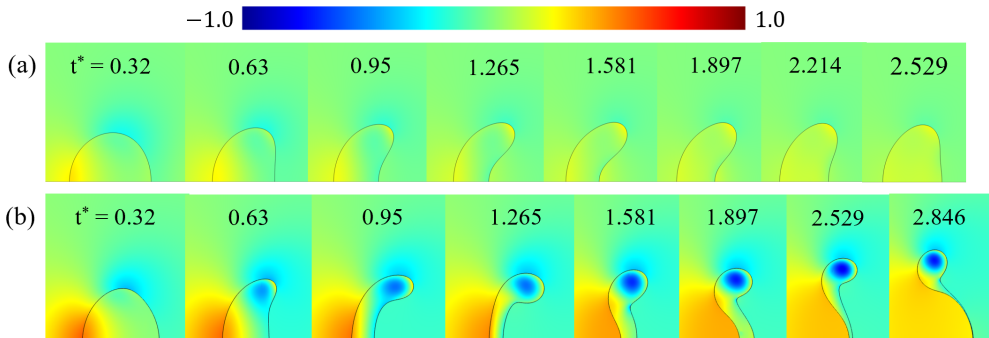


FIGURE 7. Pressure field plots are plotted for two different  $\rho$  values for a high  $Oh_o$  ambient flow. (a)  $\rho = 10$  (b)  $\rho = 1000$ . All drops shown here have the following common parameters:  $Oh_o = 0.1$ ,  $Oh_d = 0.1$ ,  $We_0 = 20$ .

central core is not fully evacuated and contains some remnant drop fluid (see  $t^* = 1.9$ ), also called a plume. A similar explanation for the formation of a plume is provided by [Jackiw & Ashgriz \(2021\)](#), where a faster bag inflation rate (due to higher  $We_0$  in the paper) compared to the movement of drop fluid from the center to rim leads to the presence of an undeformed core at the center of the drop. The volume of fluid contained in this undeformed core dictates the specific breakup observed — bag-plume, multi-bag or sheet thinning. As the drop continues to be laterally stretched, the rim gains sufficient mass by  $t^* = 1.9$  to show lower local accelerations. At this stage, the drop's rim and core start to lag behind the toroidal bag connecting the two, causing bag inflation and eventually resulting in a backward-plume bag morphology. This deformation process is also shown in [Marcotte & Zaleski \(2019\)](#) (in figure 4) for a low  $Oh_o$  case where a variation in  $\rho$  from 10 to 2000 is accompanied with a shift in pancake and breakup morphology exactly as observed here.

Let us now shift our attention to the effect of  $\rho$  on high  $Oh_o$  cases. Figure 7 shows the evolution of pressure field around the drops with time. In both cases,  $Oh_o$  is 0.1, which corresponds to  $Re_0 = 44.72$ . For such a low  $Re_0$ , we expect the shear stresses on the upstream surface to be substantial. Hence, despite observing substantially higher upstream stagnation pressures (and hence higher  $\Delta P_{drive}$ ) for (b) ( $\rho = 1000$ ) compared to (a) ( $\rho = 10$ ),  $\Delta P_{drive}$  still does not dominate over the shear stresses during pancake formation. As expected, we see a forward pancake at  $t^* = 0.948$  for both cases. Additionally, because of the low  $Re_0$  of the flow, the ambient flow remains attached to the drop's surface, eliminating the formation of any downstream circulation zones and hence any additional forcing that might have influenced the dynamics of the growing rim. Subsequently, as the drop core is evacuated and a distinct rim is formed, a backward bag remains the only possible morphology. (b) shows a backward bag breakup, while (a) shows much smaller deformations and does not fragment, the lower deformation is consistent with lower relative velocities, resulting in lower external forces.

In conclusion, the morphology of the pancake depends on the competition between the pressure difference between the poles and the periphery of the drop, with the shear stresses acting on the upstream surface. A flat pancake is observed when  $\Delta P_{drive}$  is dominant, whereas a forward-facing pancake is observed when shear stresses are dominant. As the drop deforms past the pancake stage, it forms a bag, which can be forward or backward, depending on the local inertia of the rim and the strength of the downstream vortex. Local inertia depends on  $\rho$  and the rate of evacuation of fluid from



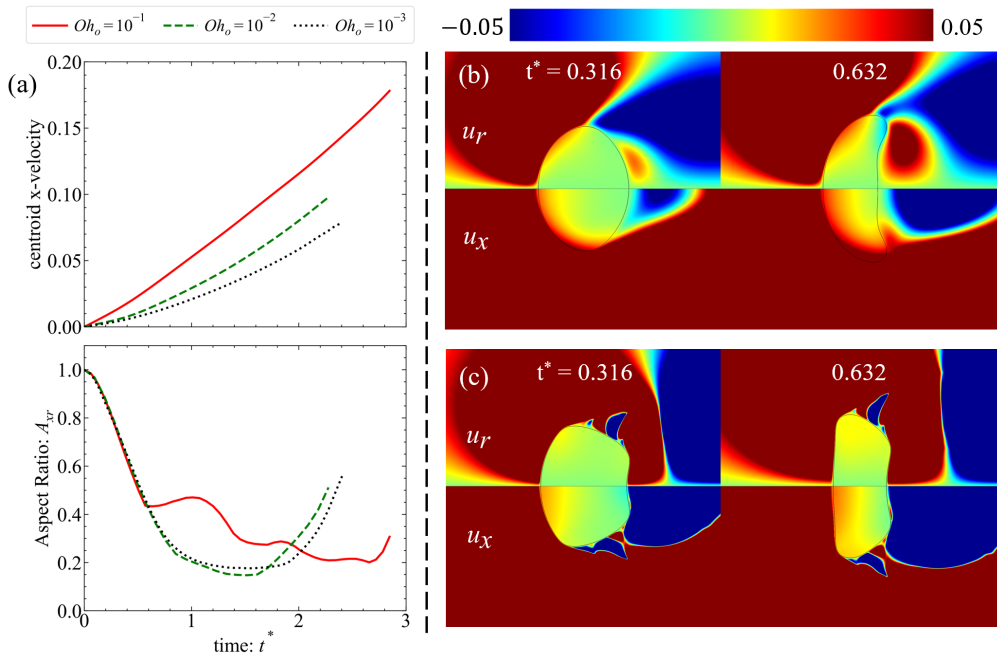


FIGURE 8. For all plots,  $\rho = 1000$ ,  $Oh_d = 0.1$  and  $We_0 = 20$ . (a) shows the temporal evolution of drop centroid x-velocity and Aspect ratio for different  $Oh_o$  values. Velocity fields are plotted for  $Oh_o = 0.1$  and  $Oh_o = 0.001$  in (b) and (c) respectively.

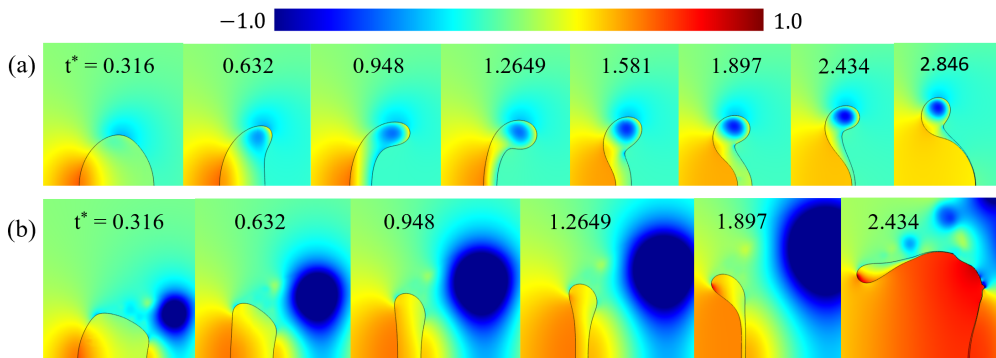


FIGURE 9. Both the drops shown here have  $\rho = 1000$ ,  $Oh_d = 0.1$  and  $We_0 = 20$ . Pressure fields are shown for drops with (a)  $Oh_o = 0.1$ , and (b)  $Oh_o = 0.001$ .

the drop core. The strength and location of downstream vortices, on the other hand, depend on  $Oh_o$  and the instantaneous centroid velocity of the drop, which again depends on inertia  $\rho$ . Finally, under conditions where the drop experiences a higher rate of lateral stretching (dependent on  $Re$ ) compared to the rate of evacuation of the core (dependent on  $\Delta P_{drive}$ ), we may also observe a plume.

### 3.2. Ambient Ohnesorge number

Figure 8(a) illustrates the impact of  $Oh_o$  on the temporal evolution of drop centroid velocities and aspect ratios, spanning  $Oh_o$  values from 0.1 ( $Re_0 = 44.72$ ) to 0.001 ( $Re_0 =$

4472). The flows with the highest values of  $Oh_o$  show the highest drop centroid velocities, attributed to the higher shear stresses in high  $Oh_o$  flows (equivalent to large ambient dynamic viscosity), and result in a larger drop centroid acceleration. As expected, a lower relative velocity results in lower stagnation pressures and lower  $\Delta P_{drive}$  values. As was seen previously in figure 5(a), all the drops also show very similar temporal development of their aspect ratios.

Pressure fields for two different  $Oh_o$  values for  $\rho = 1000$  have been plotted in figure 9. All non-dimensional parameters except  $Oh_o$  are the same for the two cases. For the drop in figure 9(a),  $Oh_o = 0.1$ , i.e.,  $Re_0$  is very low which corresponds to a large outside viscosity. This in addition to the flow not detaching from the drop surface leads to large viscous stresses on the upstream surface and consequently larger centroid velocities. The drop in figure 9(b) on the other hand has a  $Re_0$  value that is 100 times larger, leading to much smaller shear stresses and consequently smaller centroid velocities. The larger centroid velocities of the drop in case (a) leads to smaller stagnation pressures and, consequently, smaller  $\Delta P_{drive}$  compared to case (b). It should be noted that the instantaneous Reynolds number  $Re$  (instead of  $Re_0$ ) would be a more accurate descriptor of the effective shear stresses experienced by a drop. However, this discrepancy between  $Re$  and  $Re_0$  (resulting from non-zero centroid velocities and frontal radius growths) plays a minor role in influencing shear stresses compared to the two orders of magnitude change in  $Re_0$  between the two cases. For the drop shown in figure 9(a), owing to lower stagnation pressures, the shear stresses acting on its upstream surface dictate its initial internal flow and resulting deformation. This is clearly demonstrated by the internal flow plot shown in figure 8(b) for the drop, where velocities are the highest at its upstream surface and decreases to zero at its downstream pole, coinciding with the location of largest shear stresses applied by the ambient flow. This dominance of shear stresses results in the formation of a forward facing pancake.

Conversely, for the higher  $Re$  system depicted in figure 9(b), shear stresses are significantly lower, which coupled with the larger  $\Delta P_{drive}$  (compared to (a)) results in a dominant pressure internal flow. Consequently, the drop deforms into a flat pancake shape and the highest internal velocities occur at its upstream pole rather than at the periphery.

In summary, the orientation of the pancake, determined by the competition between  $\Delta P_{drive}$  and shear stresses, is influenced by both  $\rho$ , due to its significant impact on  $\Delta P_{drive}$ , and  $Oh_o$ , due to its significant impact on the  $Re$ , and consequently, the shear stresses exerted on the drop.

As the drops deform further, both cases develop a prominent rim, resulting in a large disparity in local inertia between the rim and the center (prospective bag) of the drop. In case (a), the extremely low  $Re$  results in an attached flow downstream of the drop, preventing the formation of a downstream vortex. In contrast, case (b) with its large  $Re$  develops a downstream vortex, but the large local inertia (i.e.,  $\rho$ ) allows the vortex to detach early from the drop. Hence for both cases, the rim does not experience any additional forces that can counteract the impact of the large local inertia (smaller local acceleration) of its rim. We observe that the drop in case (a) flips orientation from a forward pancake to a backward bag, while the drop in case (b) deforms from a flat pancake to a backward bag.

A decrease in ambient Ohnesorge number may also result in the breakup morphology shifting towards a more forward bag shape, particularly for lower density ratio drops. An example illustrating this effect is depicted in figure 10. Due to their intermediate  $\rho$  values, the drops show instantaneous centroid velocities somewhere between high and low  $\rho$  cases. The  $\Delta P_{drive}$  values for both cases are close to the same magnitude, yet small

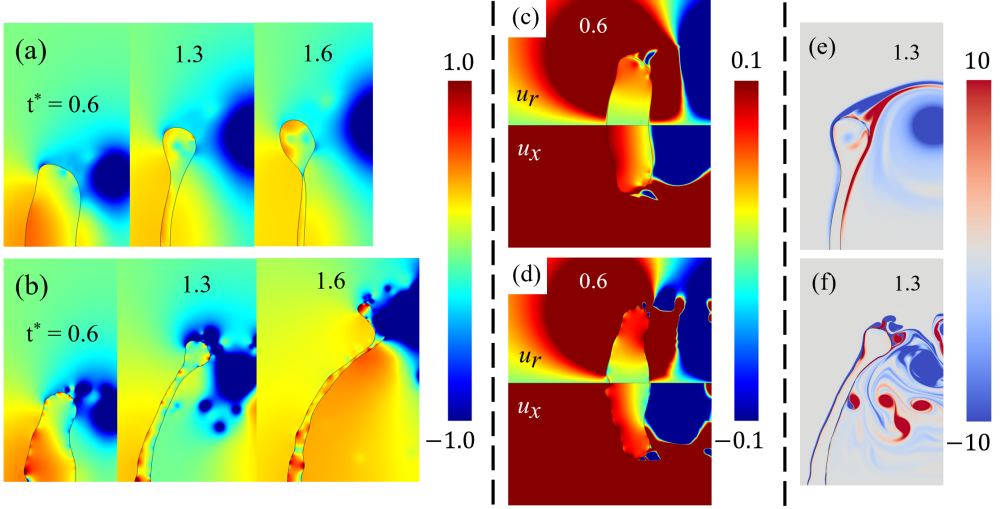


FIGURE 10. Both cases shown here have  $\rho = 100$ ,  $Oh_d = 0.001$  and  $We_0 = 13$ . (a), (c) and (e) plot pressure field, y-velocity, and vorticity for drop with  $Oh_o = 0.001$ ; whereas (b), (d) and (f) plot the same for drop with  $Oh_o = 0.0001$ .

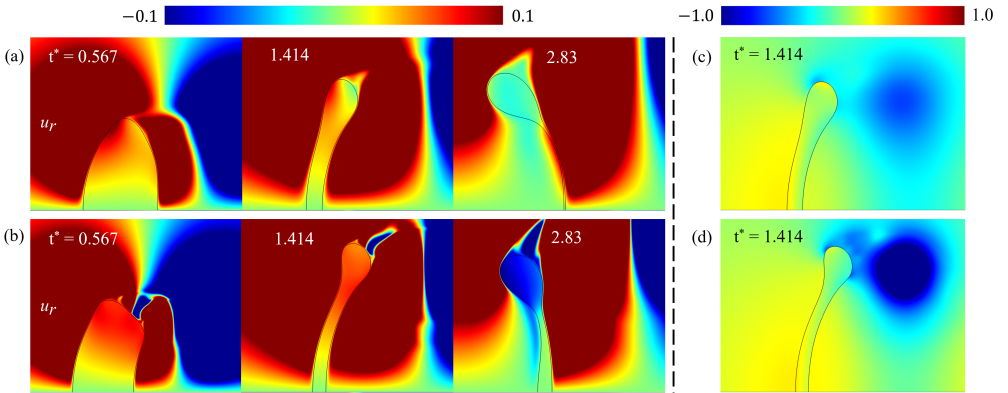


FIGURE 11. Both cases shown here have  $\rho = 50$ ,  $Oh_d = 0.1$  and  $We_0 = 20$ . (a) and (c) plot y-velocities and pressure field for drop with  $Oh_o = 0.01$ ; whereas (b) and (d) plot y-velocities and pressure field for drop with  $Oh_o = 0.001$ .

enough to not completely dominate the shear stresses acting on their upstream surfaces (similar to figure 6(b)). As a result, the pancake shapes for both cases (a) and (b) are somewhere between a forward and a flat pancake.

It is crucial to note that the case with a lower  $Oh_o$  shows a more emphasized forward bag. The reason for this can be discerned from the velocity field plots shown in figures figure 10(c) and (d) for  $t^* = 0.6$ , where the lower  $Oh_o$  case shows a higher rate of stretching from its poles to its periphery. This discrepancy in stretching rates results from differences in the downstream vortices shed by the drops. The higher  $Oh_o$  of case (a) produces a distinct solitary circulation zone, larger in size and modestly interacting with its periphery. In contrast, case (b) has its  $Re_0$  ( $\approx 36055$ ) firmly in the free shear regime (Forouzi Feshalami *et al.* 2022), producing smaller, stronger, and faster shedding vortices that form much closer to the drop periphery. Consequently, the drop in the

higher  $Re_0$  case experiences higher stretching rates from the poles to the periphery, as it is subjected to stronger induced drag forces due to better access to the low pressure zones downstream.

The increased rates of stretching seen in the two drops are not matched by the mediocre rates of evacuation of their cores, ultimately leading to the formation of a plume in both drops, creating two high inertia regions at their cores and periphery. The drop in figure 10(a) owing to its well-formed high inertia rim, flips the orientation of its bag, eventually fragmenting with a backward bag-plume morphology. On the other hand, the drop in figure 10(b) owing to its faster stretching rates, forms a larger plume, thus preventing the formation of a clear high inertia rim. As a result, its rim never escapes downstream low-pressure regions and ultimately breaks up in a forward bag morphology.

In short, the rate of stretching, and consequently the size of the resulting plume, increases with increasing proximity and strength of downstream vortices on the rim (due to increase in  $Re_0$ ). For low  $We_0$  simulations, forward bags are only observed for smaller inertia drops when  $Oh_o$  values are small, with  $Re$  preferably in the shear layer instability regime ( $1000 \leq Re_0 \leq 10^5$ ). A high density ratio case such as  $\rho = 1000$  shows forward bag breakup in current simulations only when ambient Ohnesorge number values are the smallest, i.e.,  $Oh_o = 0.0001$ .

Figure 11 shows another example in which decreasing  $Oh_o$  motivates the formation of a plume. Compared to drop (a), drop (b) shows a stronger downstream vortex due to its larger  $Re_0$ , as is evident from the y-velocity plots for the two cases, showing much larger y-velocities at its rim. Although both drops show significant lateral stretching due to their low inertia rims, the induced drag on the higher  $Oh_o$  case is larger leading to comparatively higher rates of stretching. Ultimately, the larger  $Oh_o$  case fragments with a simple backward bag breakup morphology. The lower  $Oh_o$  case instead develops a plume which leads to the formation of an annular bag between the center and the periphery, i.e. backward bag-plume morphology. As expected, none of the two cases form a forward bag since the ambient Reynolds number is too small to produce vortices in the free-shear regime.

### 3.3. Drop Ohnesorge Number

We start our investigation into the role of drop Ohnesorge number by studying cases with high density ratios and low ambient Ohnesorge numbers. In such drop-ambient systems, drops due to their large inertia maintain high relative velocities with ambient, yielding large stagnation pressures ( $\Delta P_{drive}$ ) and large instantaneous Reynolds numbers ( $Re$ ). The low shear stresses acting on its upstream surface (due to high  $Re$ ) allow  $\Delta P_{drive}$  to dictate its internal flow, resulting in the formation of a flat pancake. Given that all other nondimensional parameters are the same across two cases, the case with the larger  $Oh_d$  has a larger drop viscosity  $\mu_d$ , and is expected to have lower internal flow velocities and circulations. Higher  $\mu_d$  also results in an exponential decrease in the incidence of surface instabilities (Fuster *et al.* 2009). While an increase in surface tension decreases the wavelength of the fastest growing surface waves, an increase in  $\mu_d$  increases the length and timescales for which a capillary wave generated by an instability remains intact. As a drop accelerates and its relative velocity with ambient decreases, the effective acceleration of the drop relative to the ambient medium decreases. Consequently, a surface wave that might have been unstable at the start of deformation, might be stable at more advanced stages of deformation, under the condition that the lengthscales and timescales of instabilities are large enough for the given  $\mu_d$  (Goodridge *et al.* 1997).

Figure 13 illustrates the pressure fields for two such cases with  $\rho = 1000$ ,  $Oh_o = 0.001$ , and a varying  $Oh_d$ . Both cases show very similar (high) stagnation pressures and an

$Re_0$  of 4472 results in a well-defined downstream vortex detached from their peripheries, indicative of their large local and total inertia. As expected, at  $t^* \approx 1$ , both cases form a flat pancake and the onset of rim formation. However, for the drop in case (b), we observe a high-pressure zone at its upstream pole that hints at the initiation of a plume. The internal flow field in figure 12(b) reveals an instability at the upstream pole of the drop, motivating a flow from its periphery to its upstream pole, hugging its upstream surface. The smaller viscosity of the drop in case (b) (100 times smaller) facilitates the development of a prominent capillary instability at its pole and the corresponding pancake-plume shape. Furthermore, the location of the instability (i.e., the upstream pole) is a stagnation point and sees the highest accelerations out of all regions of the drop. This matches with the definition of Rayleigh-Taylor instabilities and might be the primary mechanism behind the development of a plume of this kind. According to Villermaux (2007); Jalaal & Mehravaran (2014), an increase in density discontinuity motivates the formation of RT instabilities. Our current simulations also show this behavior, as only the cases with  $\rho = 500$  or 1000 and for the lowest  $Oh_d$  values form an unstable plume.

As the drops in the two cases continue to deform and more mass is transferred from their cores to their rims, substantial variations in local inertia (and hence local accelerations) start to develop. Notably, for case (b), the plume has grown further and the drop now has two high local inertia regions — its core and its rim. The annular region connecting its core and rim has lower local inertia compared to both these regions and hence accelerates downstream relative to both, resulting in the growth of a bag between the plume and the rim. Ultimately, this annular bag fragments, culminating in a backward bag-plume morphology, as seen in figures for case (b).

For the drop in figure 13(b), it should be noted that a reduction in  $We_0$  (while keeping other parameters constant) still results in the development of an instability-driven plume at its upstream pole, albeit of a smaller size. For instance, when  $We_0 = 16$  for the drop in figure 13(b), it does not deform enough to exhibit fragmentation (of the bag-plume kind). Consequently, solely decreasing  $We_0$  is not sufficient to shift the breakup morphology from a backward bag-plume to simple bag breakup for the specific ( $\rho$ ,  $Oh_d$  and  $Oh_o$ ) set. This makes a backward bag-plume breakup the critical breakup morphology for this case — a feature of the physical properties of the system described by ( $\rho$ ,  $Oh_d$  and  $Oh_o$ ), and not just a function of boundary conditions (i.e., inflow velocity or  $We_0$ ).

In contrast to the plume in figure 13(b) which originates from an instability due to lack of sufficient viscous damping, a decrease in  $Oh_d$  can also lead to a plume similar to the one in figure 11(b). One such example is shown in figure 15.

If we focus our attention on the specific case of drops,  $Oh_d$  can be interpreted as the ratio of the capillary timescale  $T_\sigma$  to the viscous timescale  $T_\mu$ , i.e.,  $Oh_d = T_\sigma/T_\mu$ . The capillary timescale  $T_\sigma$  ( $= \sqrt{\rho_d D^3/\sigma}$ ) is defined as the duration for a capillary wave of wavelength  $D$  to traverse a distance of  $D$ ; while viscous timescale  $T_\mu$  ( $= \rho_d D^2/\mu_d$ ) represents the duration for momentum to diffuse across the drop (Popinet 2009). A smaller  $Oh_d$  hence implies a relatively small  $T_\sigma$  compared to  $T_\mu$ , indicating that the information about interface deformation travels much faster than the the rate of transfer of momentum to the drop fluid across the diameter. Hence, the downstream vortices could apply some induced drag on the drop rim, causing local acceleration relative to the core and, subsequent deformation. However, this induced drag may not setup equivalent flow throughout the entire drop fluid. This is evident from the y-velocity plots shown in figure 15, where the lower  $Oh_d$  case (b) shows larger y-velocities at the rim, indicating greater rates of stretching compared to the higher  $Oh_d$  case (a). Hence, case (b) due to its larger  $T_\mu$  results in a plume. It is essential to note that the drop in this case only shows

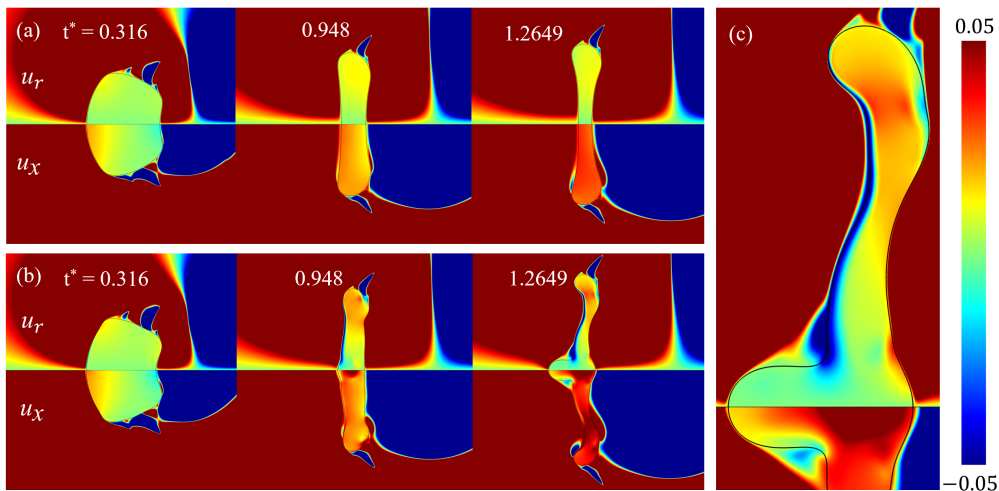


FIGURE 12. All drops in these plots have  $\rho = 1000$ ,  $Oh_o = 0.001$ ,  $We_o = 20$ . These Plots show internal flows for two different  $Oh_d$  values: (a)  $Oh_d = 0.1$ , and (b)  $Oh_d = 0.001$ . (c) is a zoomed in view of  $t^* = 1.2649$  for (b)

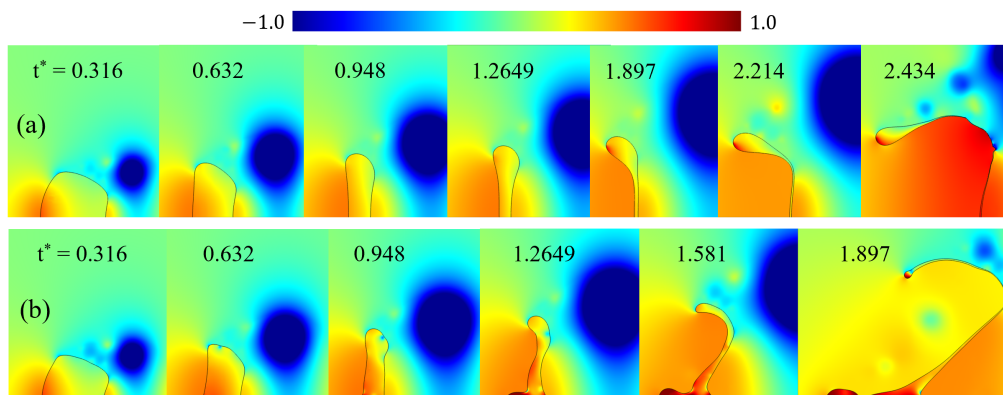


FIGURE 13. All drops in these plots have  $\rho = 1000$ ,  $Oh_o = 0.001$ ,  $We_o = 20$ . These plots show the pressure fields around drops of different  $Oh_d$  values. (a)  $Oh_d = 0.1$  (b)  $Oh_d = 0.001$ .

a plume once it has started to form a bag, and the initial pancake at  $t^* \approx 1$  is flat. In contrast, the plume in figure 13(b) develops very early in the deformation process, right at the instant of formation of the pancake. Hence, the two types of plumes fundamentally differ in their formation mechanisms.

According to much of the existing literature, if  $Oh_d \leq 0.1$ ,  $Oh_d$  tends to have minimal impact on drop breakup mechanism. Therefore, for most studies, the choice of  $Oh_d$  is not focused upon, as long as it is ensured to be lower than 0.1. However, the simulations conducted and analyzed in this study do not corroborate with this understanding.

Another example emphasizing the effect of  $Oh_d$  on drop deformation and breakup morphology is shown through drop interface plots in figure 14. In (a), the drop never achieves large enough deformation to undergo breakup. The drop in (b) on the other hand shows bag breakup for the same parameters except for  $Oh_d = 0.01$ . The lower deformations achieved by the drop (a) can be attributed to higher fluid viscosity, which

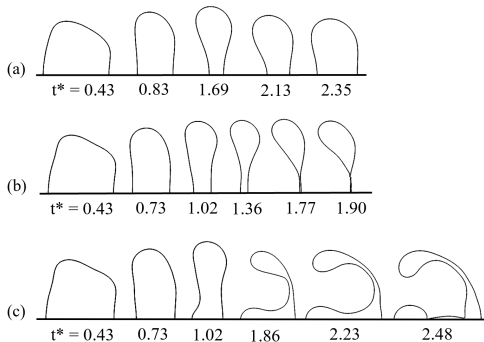


FIGURE 14. These plots show the fluid interface for three cases with  $\rho = 1000$ ,  $Oh_o = 0.001$ ,  $We_0 = 15$ , and (a)  $Oh_d = 0.1$  (b)  $Oh_d = 0.01$  (c)  $Oh_d = 0.001$ .

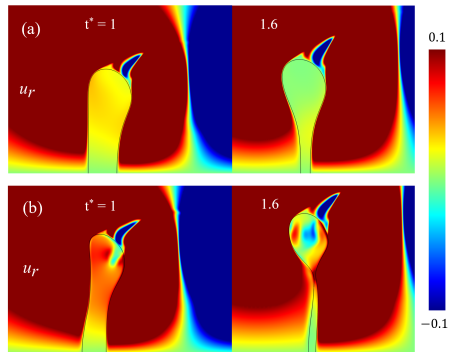


FIGURE 15. Both cases have  $\rho = 100$ ,  $Oh_o = 0.001$ ,  $We_0 = 13$ . These plots show  $y$ -velocities for two different  $Oh_d$  values: (a)  $Oh_d = 0.1$ , and (b)  $Oh_d = 0.001$ .

provides resistance to internal flow and dissipates energy supplied by the ambient flow through surface forces. For  $Oh_d = 0.001$  in (c), the breakup type shifts from a simple backward bag to a backward bag-plume breakup, with the plume formation driven by RT instabilities. In short, a decrease in  $Oh_d$  is expected to reduce the required critical Weber number  $We_{cr}$  for a backward bag breakup. Hence, for the same  $We_0 = 15$ , we observe (c) exhibit a backward bag plume breakup, which is a multimode breakup that we expect to manifest at a  $We_0$  higher than that required for a simple backward bag.

## 4. Discussion

In this work, a parameter sweep using axisymmetric simulations was performed for multiple values of Weber number for every set of  $\{\rho, Oh_o, Oh_d\}$  possible in the parameter space defined in section 2.4. From this vast set of simulation data, we set out to achieve two primary objectives: **1.** extract the influence of each involved non-dimensional parameter involved — specifically  $\rho$ ,  $Oh_o$ , and  $Oh_d$  — on drop pancake and breakup morphology; and **2.** Determine both Critical Weber number values as well as corresponding critical breakup morphologies for each unique combination of  $\{\rho, Oh_o, Oh_d\}$  in our parameter space. The first objective was addressed in detail in section 3. This section focuses on the second objective.

### 4.1. The threshold of Impulsive drop breakup

Figure 16 shows the variation of critical Weber number ( $We_{cr}$ ) against the drop Ohnesorge number ( $Oh_d$ ) for drops of different density ratios ( $\rho$ ) and the outside Ohnesorge numbers ( $Oh_o$ ).  $Oh_d$  takes three different values in the parameter space: 0.1, 0.01 and 0.001. For every  $Oh_d$ , a  $\rho$  value is represented by a colored vertical line that shows the range of  $We_{cr}$  values obtained due to variation in  $Oh_o$ . The lower  $We_{cr}$  values generally correspond to lower  $Oh_o$  values and vice versa. Therefore, for each  $Oh_d$  value in the plot, there exist 5 colored vertical lines corresponding to the 5  $\rho$  values explored in the parametric sweep. It should be noted that each colored line has been offset from its  $Oh_d$  value by a different amount for preventing overlaps with other  $\rho$  lines and hence improve clarity. All the cases are also explicitly marked with a uniquely shaped marker corresponding to each fragmentation morphology. Finally, all the experimental data for

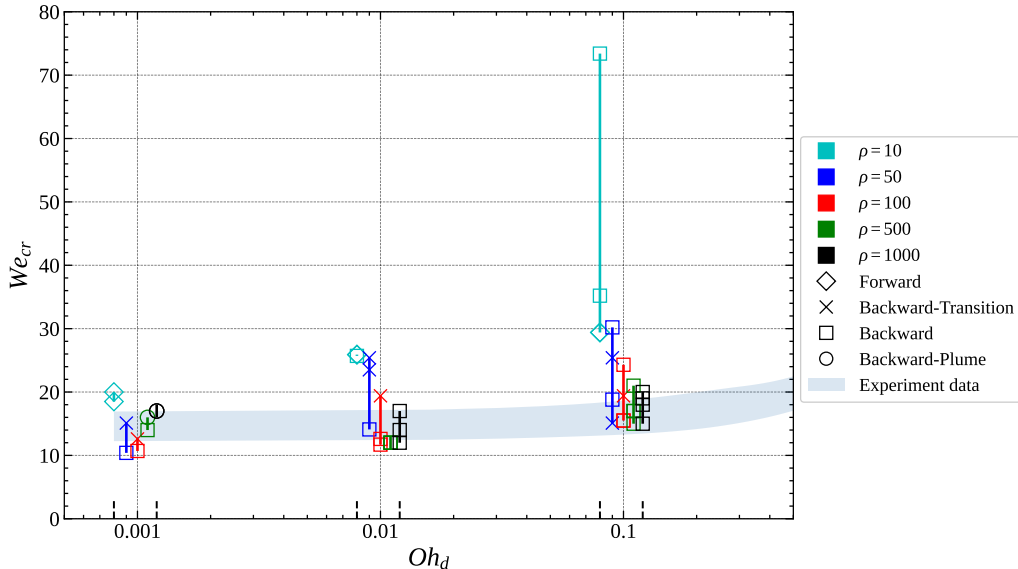


FIGURE 16. Plot of  $We_{cr}$  against  $Oh_d$ . Dependence on  $Oh_o$  is represented using vertical lines, with their vertical extent representing corresponding variation in  $We_{cr}$ . Dependence on  $\rho$  is shown through different colored vertical lines (offset from its true x-location to prevent overlaps with other lines) representing each  $\rho$  value in the parameter space. Specific markers are used to represent all critical breakup morphologies observed in the simulations.

$We_{cr}$  explored through this work is shown as a translucent area in the background of the plot, also shown as explicit markers in figure 1.

On the basis of all the simulation results and figure 16, the following conclusions emerge:

(i) **Consistency with experimental data:** All simulations with high  $\rho$  ( $\geq 500$ ) values critically fragment at  $We_{cr}$  values that very closely match historical experimental works. This is expected given that most experimental studies have historically focused on impulsive fragmentation for water-air analogous systems, which have  $\rho \geq 500$ . Only cases with  $\rho < 500$  show any appreciable deviation from the experiments.

(ii) **Sensitivity to  $Oh_o$ :** The lowest  $\rho$  cases exhibit the largest variations in critical Weber numbers with respect to changes in  $Oh_o$  for the high  $Oh_d$  cases, as indicated by the length of vertical lines in figure 16. A drop with a large  $\rho$  ( $\geq 500$ ) experiences larger relative velocities, making  $\Delta P_{drive}$  the dominant factor driving its deformation in most cases. Even in cases with large external shear stresses on the drop (the largest  $Oh_o$  cases), once a clear rim has formed in the deformed drop, local inertia variations take over the deformation process. Only the lower inertia ( $\rho$ ) drops show the any appreciable sensitivity to changes in  $Oh_o$  and the corresponding differences in downstream vortical structures. An exception exists when  $Oh_o$  is in the free-shear regime ( $Re_0 > 10000$  (section 3.2), and even the drops with a high  $\rho$  respond strongly to the resulting downstream vortices, fragmenting with a forward bag morphology.

(iii) **Variations in fragmentation morphologies:** The critical breakup morphology transitions from a forward bag ( $\rho = 10$ ) to a backward-transition ( $\rho = 50, 100$ ) (see figure 17) to a backward and backward-plume bag with increase in  $\rho \geq 500$ . As  $\rho$  increases, the drop's rim is expected to start lagging behind the drop core at some point during its deformation, when local inertia of its rim becomes substantially larger than that of its core. The shift in morphology from a forward to a backward bag is observed



only for low  $Oh_o$  values, which produce downstream vortices that are strong enough to compensate for the larger local inertia of the rim. Alternatively, large  $Oh_o$  cases always exhibit backward bag breakup at critical conditions. This is due to the downstream vortices being weak or non-existent for low  $Re_o$  flows.

(iv) **Sensitivity to  $Oh_d$** : In addition to drop Ohnesorge number's role in controlling the sensitivity of  $We_{cr}$  to  $Oh_o$ , a decrease in  $Oh_d$  also affects the critical fragmentation morphology by motivating the formation of a plume. This is seen for the lowest  $Oh_d$  (0.01, 0.001) and  $Oh_o$  (0.001, 0.0001) values, and for the largest  $\rho$  (500, 1000) drops (star shaped marker in figure 16). Such drops show an unstable plume at the upstream poles of their flat pancakes, which are also locations of maximum acceleration in the drops and can be attributed to Rayleigh-Taylor instabilities. Both low viscosity and larger density ratios motivate the development of such instabilities (Villiermaux 2007; Gueldenbecher *et al.* 2009; Jalaal & Mehravaran 2014). Since the pancake for this non-dimensional set starts with a plume even for lower non-critical  $We_o$  values, a plain backward bag breakup can never manifest for such systems, and hence a backward bag-plume breakup becomes its critical breakup morphology.  $Oh_d$  also influences the rate of evacuation of the drop core, which ultimately results in a forward bag for all high  $Oh_o$  cases, when shear stresses drive pancake formation.

The conclusions drawn from figure 16 show that the accepted idea of critical Weber number being almost independent of drop Ohnesorge number for  $Oh_d < 0.1$ , might not always hold, especially for systems that stray too far from properties analogous to Water-Air. Furthermore, the critical breakup morphology need not necessarily be a backward bag breakup. Backward bag-plume and forward bag morphologies can be the critical morphologies for certain low  $\rho$  and low  $Oh_o$  cases.

A path diagram, as illustrated in figure 17(a), can be drawn that summarizes all the deformation paths a spherical drop might follow as it deforms to critical fragmentation under impulsive acceleration. A companion phase diagram (figure 17(b)) provides the non-dimensional parameter space that results in one of the four observed fragmentation morphologies. It is worth highlighting that all the breakup paths provided in the diagram are for their respective critical conditions, and consequently the  $We_{cr}$  values corresponding to different paths need not be the same.

For small  $\rho$  or high  $Oh_o$  values or both, shear stresses drive the internal flow, resulting in a forward pancake. The fate of this forward-facing orientation is then contingent on the balance between local inertia differences and the strength and proximity of downstream vortices to the rim. For systems with large  $Oh_o$ , irrespective of density ratio, downstream vortices either do not form or shed further downstream. The drop is not subjected to large lateral stretching rates, allowing the formation of a prominent toroidal rim. The resulting lateral inertia differences lead to the flipping of the bag from forward to backward orientation, eventually fragmenting with a backward bag morphology. On the other hand, for small  $Oh_o$  (and hence small  $\rho$  for a forward pancake) coupled with large  $Oh_d$ , the strong, fast, and proximal downstream vortices generate large lateral stretching rates, preventing the formation of a prominent rim. As a result, the drop continues to hold its forward facing orientation and breaks up with a forward bag morphology.

When  $\rho$  is large and  $Oh_o$  is small, the drop under critical conditions either deforms into a flat pancake or a flat pancake with a plume depending on whether  $\rho$  and  $Oh_o$  are at the extreme ends of the parameter space. The largest values of  $\rho$  and the smallest values of  $Oh_o$  and  $Oh_d$  lead to the appearance of a plume at the upstream pole of the flat pancake. It can be hypothesized that the low viscosities of both outside and drop fluids do not provide sufficient viscous dissipation to stabilize the jet ejected at the upstream pole (due to Rayleigh-Taylor instability) of the drop. From this pancake

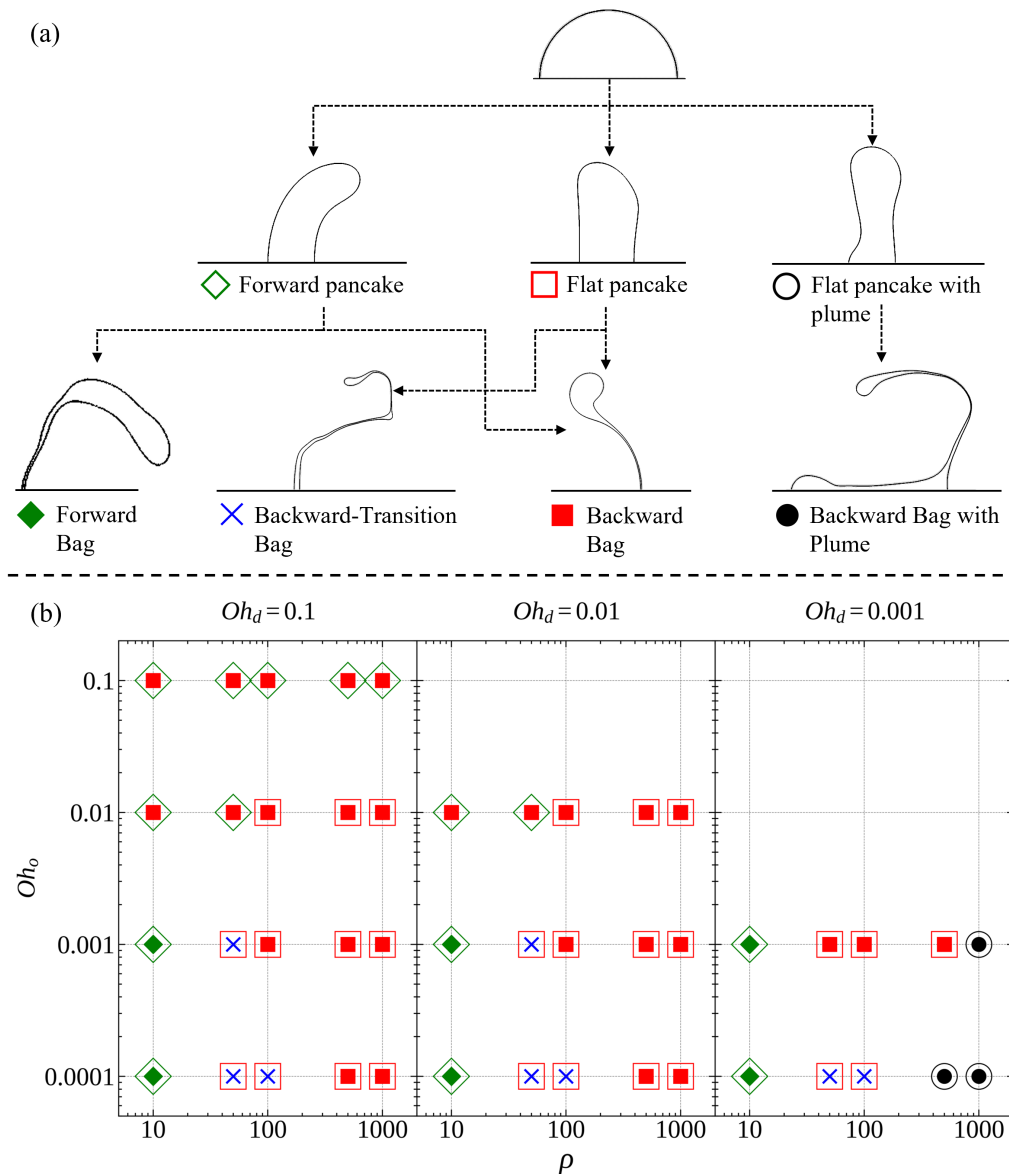


FIGURE 17. (a) is a path diagram of all deformation paths a spherical drop under impulsive acceleration can take when breaking up critically. A spherical drop can deform into three types of pancakes, each of which can further deform into one of four breakup morphologies, the corresponding  $\rho$ ,  $Oh_o$ ,  $Oh_d$ ,  $We_0$  parameter space is shown in the phase diagram (b).

shape, the only possible critical breakup morphology is a backward bag-plume breakup. All other intermediate cases form a flat pancake which can form either a backward-transition breakup (for intermediate  $\rho$  values and low  $Oh_o$  values) or a backward bag (for all the remaining cases). A backward-transition breakup is a forward bag with a flipped rim, i.e. a drop which at its final moments gains enough inertia in its rim to start the bag flipping process. As expected, this is observed for intermediate  $\rho$  values where

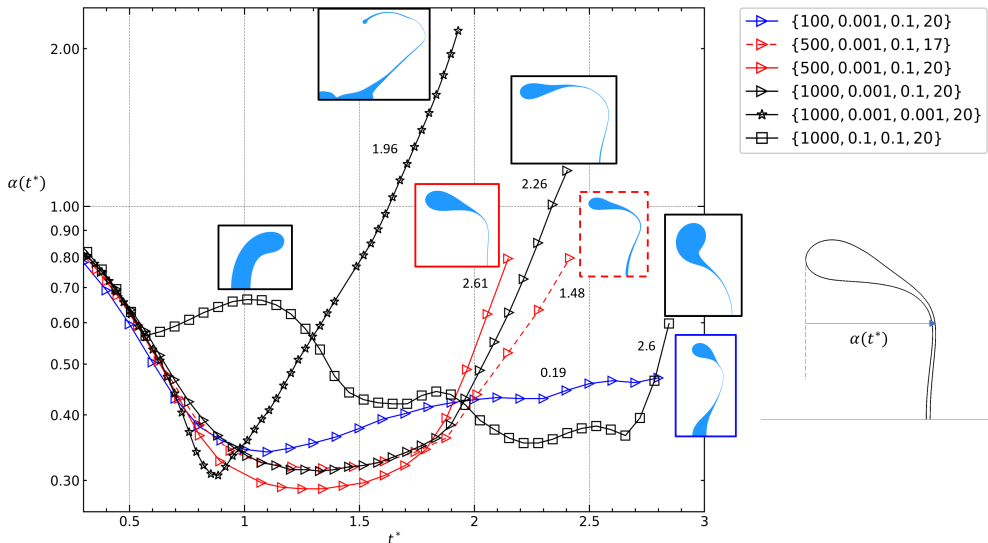


FIGURE 18. Bag inflation  $\alpha(t^*)$  with time  $t^*$  is shown for some unique backward bag breakup cases. The non-dimensional parameter set for each case is of the form  $\{\rho, Oh_o, Oh_d, We_0\}$ . The cases plotted here include simple backward bags ( $\{500, 0.001, 0.1, 17\}$ ,  $\{1000, 0.1, 0.1, 20\}$ ,  $\{1000, 0.001, 0.1, 20\}$ ) and backward plume-bags ( $\{100, 0.001, 0.1, 20\}$ ,  $\{500, 0.001, 0.1, 20\}$ ,  $\{1000, 0.001, 0.001, 20\}$ ). In addition,  $\{1000, 0.1, 0.1, 20\}$  initially forms a forward pancake shape which then flips to backward bag. Through this plot, the effect of  $We_0$ ,  $Oh_o$  and  $\rho$  on bag inflation rates is highlighted.

neither local inertia differences nor downstream vortices outright dominate the dynamics of the drop's periphery.

The path diagram, together with the phase diagram, only informs of the types of pancakes and corresponding general breakup morphologies observed for a specific set of  $\{\rho, Oh_o, Oh_d\}$  under threshold conditions. For information on the lowest  $We$  required to achieve the corresponding non-vibrational breakup (i.e.  $We_{cr}$ ), one may refer to figure 16.

#### 4.2. Bag Inflation Characteristics

An understanding of the timescales involved for the inflation of bags during bag breakups is essential in correct estimation of bag burst timescales and effective centroid velocities for bag breakups. [Villermaux & Bossa \(2009\)](#) were the first to give an analytical description of bag inflation rates for backward bag morphology. They found that the amplitude of bag inflation increased exponentially with time with an exponent factor of 2 for an inviscid drop. [Kulkarni & Sojka \(2014\)](#) extended the work of [Villermaux & Bossa \(2009\)](#) to include drop viscosity and numerically obtained a similar exponential relationship for bag inflation, now also dependent on  $Oh_d$ . However,  $Oh_d$  was found to have a very small impact on bag inflation rates.  $We_0$  on the other hand has a more dramatic effect on the exponent factors governing inflation, with higher  $We_0$  showing faster inflation rates. The large variety of simulations in the current work across a large parameter space present an opportunity to explore the role of the relevant non-dimensional parameters on bag inflation.

The evolution of bag inflation  $\alpha(t^*)$  with time for a few backward bag simulations are illustrated in figure 18, where  $\alpha(t^*)$  is equal to the horizontal extent of the drop  $e_x$  (as shown in figure 4). For every plot, the drop shows a decrease in  $\alpha(t^*)$  up until it reaches

the end of pancake stage at  $t^* \approx 1$ , beyond which the drop begins to inflate. The only exception is the  $\{1000, 0.1, 0.1, 20\}$  case, which initially shows an increase in  $\alpha(t^*)$  due to deforming to a forward pancake. Bag inflation stage only starts at  $t^* \approx 2.5$  for this case. Once firmly in the bag inflation stage, all cases plotted here show an exponential growth  $\alpha(t^*)$  with time with a specific exponential growth factor, marked in figure 18 as numbers alongside each plot.

From the plots, a number of key observations can be made. The  $\{1000, 0.001, 0.001, 20\}$  case, which has properties closest to a water-air drop-ambient system, shows an inflation growth factor of 1.96, which is very close to the value that was analytically found by Villiermaux & Bossa (2009), and was matched against a bag breakup experiment of a water drop. Even though this case is a Backward-plume breakup, its inflation growth rate matches that of a simple bag and is not affected by the presence of the plume.

For  $\{500, 0.001, 0.1\}$  case, out of the two Weber numbers shown in the plot ( $We_0 = 17, 20$ ), the higher  $We_0$  drop shows a faster bag inflation rate, indicated by the larger exponential growth of its  $\alpha(t^*)$ . This is an expected observation, since the overall deformation rate is also higher for a higher  $We_0$  case, owing to the lower surface tension forces relative to the dynamic pressure forces driving the drop's deformation. Hence, the same amount of energy (supplied to the drop by the external forces) should lead to a larger change in the interface area as a result of a lower surface tension.

We also observe that the  $\rho = 100$  case shows a dramatically lower inflation rate compared to an analogous  $\rho = 500$  or  $\rho = 1000$  cases. This may be attributed to the lower relative velocities with ambient observed for the low  $\rho$  case, which results in a decrease in its effective Weber number, and hence lower bag inflation rates.

drop and ambient viscosities appear to have an inverse effect on bag inflation rates. Among the three  $\rho = 1000$  cases shown in the plot, the higher drop and ambient Ohnesorge number cases show the larger exponential growth rates of  $\alpha(t^*)$ .

More generally, figure 18 shows that  $t \approx \tau$  (or  $t^* \approx 1$ ) is a good representative timescale for the start of the bag inflation process. This observation is consistent with the aspect ratio plots shown in figures 5 and 8, where the pancake formation stage almost always ended at  $t^* \approx 1$ .

If the aerodynamic forces acting on a drop are large enough to initiate bag inflation in its pancake, it is expected that the drop will go on to or be very close to fragmentation. Therefore, we hypothesize that the balance of all forces acting on a drop at this stage (aerodynamic forces driving its deformation, and capillary and viscous forces resisting it), i.e., at the end of its pancake formation and at the start of its bag inflation, is representative of the overall stability of the drop fragmentation process. We will use this understanding to obtain a better estimate of the effective aerodynamic forces on the drop in the next section.

### 4.3. A parameter for Prediction of Breakup Threshold

Most previous studies have characterized the threshold for impulsive breakup of spherical drops using a Weber number based on the initial relative velocity with ambient ( $We_0 = \rho_o V_0^2 D / \sigma$ ). For all cases with properties analogous to water-air system, i.e.,  $\rho > 500$ ,  $Oh_o < 0.01$  and  $Oh_d < 0.1$ , critical breakup occurs consistently at a critical Weber number of  $We_{cr} \approx 14$ . However, as has been discovered and exhaustively described through the simulation results in the previous sections (summarized succinctly in figures 16 and 17), different cases which stray away from the non-dimensional space described by water-air systems do not show the same threshold Weber number value. Substantially higher  $We_{cr}$  values are observed for cases with low density ratios and high Ohnesorge numbers. Weber number  $We_0$  represents the ratio of the pressure forces

applied on a drop surface by the ambient medium, based on its initial relative velocity to the surface tension acting against any change in surface energy. However, drop deformation also depends on the viscous forces applied by the surrounding flow, the inertia and hence the acceleration, and the viscous dissipation against internal fluid flow. These effects have been explained in detail in section 3 through simulations for varying  $Oh_o$ ,  $Oh_d$  and  $\rho$  values respectively.  $We_0$  hence does not capture the role of all the factors relevant in the drop deformation process. We aim to construct a new non-dimensional group which aggregates the effect of all the parameters, namely  $We_0$ ,  $Oh_o$ ,  $Oh_d$ , and  $\rho$ , and shows a consistent critical value demarcating the threshold of breakup under impulsive acceleration for the complete parameter space explored in this study.

Let us assume that this new non-dimensional number, denoted by  $C_{breakup}$ , is a function of all the dimensional variables involved in the breakup process (4.1). There are 3 independent dimensions in the problem. Hence, through Buckingham-Pi analysis, we can obtain at most 4 independent non-dimensional numbers. The 4 non-dimensional numbers relevant to this problem have already been defined in section 2.1, namely  $\rho$ ,  $Oh_o$ ,  $Oh_d$ , and  $We_0$ . So, it is expected for  $C_{breakup}$  to be a function of these parameters (4.2).

$$C_{breakup} = f(V_0, D, \rho_o, \rho_d, \mu_o, \mu_d, \sigma) \quad (4.1)$$

$$C_{breakup} = f(We_0, \rho, Oh_o, Oh_d) \quad (4.2)$$

To obtain  $C_{breakup}$ , we follow a procedure similar to that employed by Blackwell *et al.* (2015) (see section IV), where they used the ratio of the forces antagonistic to each other to define a non-dimensional group. We utilize a similar hypothesis to define  $C_{breakup}$ , i.e., the competition between the forces driving drop fluid from its core to its periphery, and the forces resisting this flow, to define a criteria for the threshold of secondary fragmentation. The forces will be evaluated at  $t^* \approx 1$ , which represents the end of the pancake stage and the start of the bag inflation process. The choice of  $t^* \approx 1$  as the critical time controlling the bag inflation process has been justified in section 4.2.

$$C_{breakup} = \frac{\text{Forces driving drop deformation}}{\text{Forces resisting drop deformation}} \quad (4.3)$$

Let us assume that a spherical drop of diameter  $D_0$  at  $t^* = 0$  deforms in to a disk of diameter  $D$ , bounded radially by a semi-circular ring of diameter  $W$ , and has an aspect ratio  $A_{xr}$  at  $t^* = 1$  (figure 19(a)). Mass conservation when applied to the drop gives us  $D \approx (2/A_{xr})^{(1/3)}D_0$  and  $W \approx (2/3)(D_0^3/D^2)$ , if we ignore the mass that the curved periphery holds.

All regions of the pancake within the flat disk region ( $r < D$ ) have a very large local radius of curvature, and hence contribute negligibly to surface tension forces locally. The periphery is the only region with any appreciable curvature equal to the sum of local longitudinal and azimuthal curvatures, i.e.,  $(2/W + 2/D) = 2(1 + A_{xr})/W$ . Therefore, crossing the drop interface at its periphery produces a pressure jump of  $2\sigma(1 + A_{xr})/W$  according to the Young-Laplace equation, that acts on the narrow cylinder between the semi-circular peripheral ring and the flat disk of area  $\pi DW$  at a radial distance  $D/2$  (point 2 in figure 19(a)). The entire contribution of surface tension, directed against the movement of the drop fluid from the core to the periphery, can then be estimated by calculating the force applied by the excess pressure on this area.

$$F_\sigma = 2\pi\sigma D(1 + A_{xr}) \quad (4.4)$$

If the flow around the pancake is assumed to be a potential flow with a stagnation

point at the upstream pole, the pressure at the upstream surface of the pancake at radial distance  $r$  from the longitudinal (axisymmetric) axis can be estimated (Villermaux & Bossa 2009; Jackiw & Ashgriz 2021) as:

$$p_o(r) = p_o(0) - \frac{\rho_o a^2 V_{rel}^2 r^2}{8D_0^2} \quad (4.5)$$

$p_o(0) = 0.5\rho_o V_{rel}^2$  is the stagnation pressure at the upstream pole, and the pressure drops as we move radially away from the upstream stagnation point towards the periphery. The potential flow around a rigid body has a stretching factor  $a$  of 6 for a sphere and  $4/\pi$  for a flat disk, the latter being applicable in this work for the flow around a flat pancake. The true pressure inside the drop is a superposition of aerodynamic pressures and excess pressure due to surface tension. Since the local curvature of the drop interface is negligible for  $0 < r < (D - 0.5W)$ , the pressure inside the drop  $p_d(r)$  near its upstream surface in the disk region is almost equal to  $p_o(r)$ . Therefore, we can calculate the independent contribution of the aerodynamic pressure forces in driving the evacuation of the drop core — by integrating the infinitesimal force due to  $p_o(r)$  acting on a cylindrical surface of radius  $r$  and width  $W$  across the radius of the pancake.

$$F_p = \int_0^{0.5D} [p_o(r)(2\pi rW) - p_o(r+dr)(2\pi(r+dr)W)] \quad (4.6a)$$

$$= -2\pi W \int_0^{0.5D} \left[ p_o(r) + \frac{\partial p_o(r)}{\partial r} r \right] dr \quad (4.6b)$$

$$F_p = \frac{a^2}{48} \pi \rho_o V_{rel}^2 D_0 D - \frac{1}{3} \pi \rho_o V_{rel}^2 \frac{D_0^3}{D} = F_{p,d} - F_{p,s} \quad (4.7)$$

$F_{p,d}$  is the contribution of the radial pressure drop in the ambient flow in support of evacuation of the core, whereas  $F_{p,s}$  is the contribution of stagnation pressure against it.

In addition to surface tension and external dynamic pressures, we must estimate the contribution of drop fluid viscosity in dissipating (part of) the kinetic energy of the internal flow. An estimate for the differential viscous dissipation power can be obtained by using the following relation (Batchelor 1967; Deville *et al.* 2002; Rimbart *et al.* 2020):

$$\Phi = 2\mu_d \mathbf{d} : \mathbf{d} = 2\mu_d d_{ij} d_{ij} \quad ; \quad \mathbf{d} = \frac{1}{2} [\nabla \mathbf{u} + (\nabla \mathbf{u})^T] \quad (4.8)$$

$\mathbf{d} : \mathbf{d}$  is the dyadic product of the rate of deformation tensor  $\mathbf{d}$ , and  $\mathbf{u}$  is the velocity vector of internal flow in the pancake. Using mass conservation, Kulkarni & Sojka (2014) derived a relation  $u_r = r\dot{D}/D$  for the radial velocity of the drop fluid in terms of its radial expansion rate, which in Cartesian coordinates can be written as  $\mathbf{u} = (\dot{D}/D)(x\hat{\mathbf{j}} + y\hat{\mathbf{k}})$ , given that the transverse plane is synonymous with the  $yz$ -plane. Substituting this velocity function in equation 4.8 and dividing by the local velocity scale, we can obtain a scale for the small local viscous force, which is always oriented in a direction opposite to the internal flow velocity (i.e., negative radial direction).

$$dF_\mu \propto 4\mu_d \frac{\dot{D}}{D} \frac{1}{r} \quad (4.9)$$

Integrating equation 4.9 over the entire volume of the pancake, we get an estimate for the total viscous dissipation force working against the internal flow.

$$F_\mu \propto \frac{4}{3} \pi \mu_d D_0^3 \frac{\dot{D}}{D^2} \quad (4.10)$$

A drop under impulsive acceleration starts at zero velocity and then asymptotically

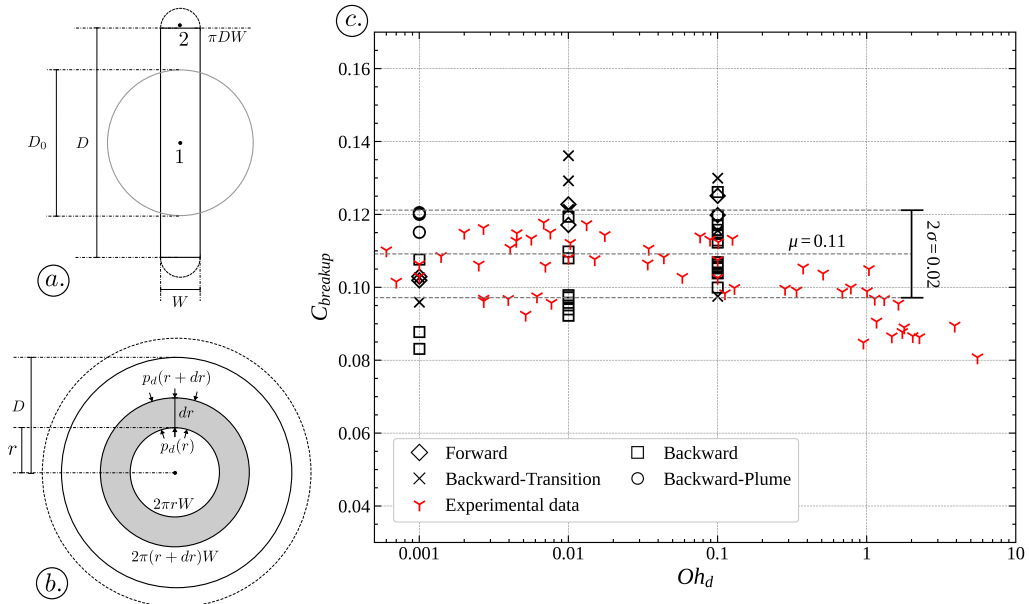


FIGURE 19. This figure shows an alternate version of figure 16 where instead of  $We_{cr}$ , the variation of  $C_{breakup}$  with respect to  $\rho$ ,  $Oh_o$ , and  $Oh_d$  is plotted. In addition to simulation data, all available experimental data in the relevant non-dimensional space for critical bag breakup (plotted in figure 1) is also plotted here for reference.

accelerates towards a maximum velocity equal to that of the ambient flow (given that the drop is still intact). This acceleration is driven by the pressure and viscous stresses applied by the outside flow on the drop interface, the corresponding magnitude of which is dictated by the instantaneous Reynolds number and relative velocity with the ambient medium  $V_{rel}$ .

As the drop continues to accelerate, its relative velocity with respect to the ambient medium continues to decrease, which reduces both the pressure and the viscous stresses. For water-air systems where  $Oh_o$  is low and  $\rho$  is high, the drop does not show significant accelerations and  $V_{rel}$  remains close to the initial relative velocity of  $V_0$  for almost the entire duration of the breakup process. For such cases, setting  $V_{rel}$  equal to  $V_0$  would be a valid assumption. Conversely, if the drop shows significant accelerations and gains velocities that are a substantial fraction of  $V_0$  (which is the case for low  $\rho$  or high  $Oh_o$  systems),  $V_{rel}$  cannot be assumed to be equal to  $V_0$  anymore. It then becomes essential to derive a scaling for  $V_{rel}$  that is valid for the whole parameter space. For this purpose, we make use of the drag equation for a sphere (4.11) to obtain a scale for the acceleration experienced by the drop.

$$F_{drag} = \frac{1}{2} C_D \rho_o V_{rel}^2 A \quad (4.11)$$

At  $t = 0$  when the drop is at rest:

$$\rho_d \frac{\pi}{6} D^3 a_0 = F_{drag}(t = 0) = \frac{\pi}{8} C_{D0} \rho_o V_0^2 D^2 \quad (4.12a)$$

$$\therefore a_0 = \frac{3}{4} \frac{1}{\rho D} C_{D0} V_0^2 \quad (4.12b)$$

Using the acceleration scale  $a_0$ , we obtain a scale for the centroid velocity of the drop

by finding the velocity after a time of the order of the deformation timescale  $\tau$  has elapsed (section 4.2), denoted as  $V_\tau$ .

$$V_\tau \propto \tau a_0 \propto \left( \frac{D}{V_0} \sqrt{\rho} \right) \frac{3}{4} \frac{1}{\rho D} C_{D0} V_0^2 = \frac{3}{4} \frac{C_{D0}}{\sqrt{\rho}} V_0 \quad (4.13)$$

A scale for  $V_{rel}$  can be obtained by evaluating  $V_0 - V_\tau$ :

$$V_{rel} \propto V_0 \left( 1 - \frac{3}{4} \frac{C_{D0}}{\sqrt{\rho}} \right) = K_v V_0 \quad (4.14)$$

In figures 5 and 9, we observe that the drop's centroid velocity decreases with an increase in  $\rho$  and a decrease in  $Oh_o$ . These observations are in line with the relative velocity scale obtained in equation (4.14), where  $C_{D0}$  is a function of  $Re_0 = \sqrt{We_0}/Oh_o$ . Any increase in the ratio between  $C_{D0}$  and  $\sqrt{\rho}$  leads to a decrease in  $V_{rel}$ .

$\dot{D}$  is estimated to be equal to  $2V_{rel}/(\sqrt{\rho} + 1)$ , described as Dimotakis velocity (Dimotakis 1986) and also used by Marcotte & Zaleski (2019) in their work. Finally, in all simulations conducted in the current work across the parameter space, it was observed that the aspect ratio  $A_{xr}$  at  $t^* \approx 1$  was almost always 0.175, and we will use this value and the corresponding  $D$  for the calculation of the forcing scales.

At this stage, we have derived all the relevant forcing scales and related parameters for deriving a new parameter describing fragmentation threshold. However, this derivation hinges upon an important assumption that the pancake is a flat disk for all the cases. This is however not true for all the high  $Oh_o$  cases which form a forward facing pancake (concave shape pointing downstream). This difference in geometry affects the potential flow and the corresponding pressure field around the drop, the pressure jumps due to surface curvature, and the corresponding internal flow vectors.

It is also important to note that the use of the deformation time scale  $\tau$  to estimate the velocity scale implicitly inherits the assumption that the drop flattens into a pancake in time  $\tau$ , and the balance of forces acting on the drop control whether the pancake invariably develops a bag. Hence, we expect  $C_{breakup}$  to correctly capture the threshold only for drops that go through a critical pancake shape during their deformation process.

Equation 4.3 can now be rewritten incorporating the pressure deficit and stagnation pressure forces (4.7), surface tension force (4.4), and viscous resistance in drop fluid (4.10).

$$C_{breakup} = \frac{F_{p,d}}{F_{p,s} + F_\sigma + F_\mu} \quad (4.15)$$

which finally results in:

$$C_{breakup} = \frac{(a^2/48) We_0 K_v^2 D^2}{2D^2(1 + A_{xr}) + (4/3) Oh_d (\rho We_0)^{0.5} \dot{D} + (1/3) We_0 K_v^2} \quad (4.16)$$

For a water-air analogous systems,  $Oh_d \ll 1$  and  $\rho > 500$ , which implies that  $K_v \approx 1$  ( $C_{D0} \approx 1$  for large  $Re_0$ ) and  $\dot{D} \approx V_{rel}/\sqrt{\rho}$ .  $C_{breakup}$  can then be simplified to:

$$C_{breakup} = \frac{(a^2/48) We_0 D^2}{2D^2(1 + A_{xr}) + (1/3) We_0} \quad (4.17)$$

For obtaining  $C_{breakup}$  using 4.16, an explicit equation for drag coefficient is required. We use the relationship (4.18) provided by Turton & Levenspiel (1986). Note that  $C_{D0}$  is a function of  $Re_0$  but can also be expressed in terms of  $Oh_o$  and  $We_0$  since  $Re_0 = \sqrt{We_0}/Oh_o$ .



$$C_{D0} = \frac{24}{Re_0} (1 + 0.173 Re_0^{0.657}) + \frac{0.413}{1 + 16300 Re_0^{-1.09}} \quad (4.18)$$

The  $We_{cr}$  vs  $Oh_d$  plot in figure 16 is recreated using  $C_{breakup}$  (4.16) in the y-axis in figure 19(c). When scaled according to this new non-dimensional parameter, almost all simulation points move to a narrow range of  $0.083 < C_{breakup} < 0.137$  with a standard deviation of 0.02 about a mean of 0.11, when compared to  $10 < We_{cr} < 74$  in the former plot. The highest  $We_{cr}$  cases corresponding to  $Oh_d$  and  $Oh_o = 0.1$  and  $\rho = 10, 50$  in figure 16 when plotted according to 4.16 achieve substantially lower threshold values, much more in line with the  $C_{breakup}$  values obtained for other simulation cases. It is also observed that the non-trivial fragmentation morphologies such as backward bag-plume and backward-transition breakup cases show relatively the largest  $C_{breakup}$  values among all other cases with the same  $Oh_d$ .

We also plot  $C_{breakup}$  values of all the available experimental data for critical backward bag breakup as a set of reference data for the plot. As expected, the experimental data remains bound within a narrow extent of  $C_{breakup}$  values, similar to its  $We_{cr}$  analog. The  $C_{breakup}$  values do start to drop off as we approach larger and larger  $Oh_d$  values, i.e.,  $C_{breakup}$  appears to overestimate the effort required to achieve critical breakup in very high  $Oh_d$  drops compared to experiments. This is in line with the observations in previous experimental works (Hinze 1955; Hsiang & Faeth 1995) where it was observed that bag breakup becomes progressively difficult for higher drop Ohnesorge numbers and ultimately stops manifesting for  $Oh_d > 2$ . Other breakup modes such as multimode and sheet-thinning become the critical breakup modes for very high  $Oh_d$  systems. The inherent assumption in the derivation of  $C_{breakup}$  was to assume that critical breakup morphology is a bag breakup, i.e., a drop first flattens into a pancake which then blows in to a bag. Any major deviation from this general breakup mechanism is expected to drastically change the deformation and breakup physics of such drops. Hence, as  $Oh_d$  increases past 1, physics related to multimode and sheet thinning breaks starts to become significant and hence must be considered in the derivation of any parameter attempting to define the critical breakup criteria.

Another factor worth considering is the initial Reynolds number required (i.e.,  $Re_0 = \sqrt{We_0/Oh_o}$ ) for very large  $We_0$  values to show a breakup for high  $Oh_d$  drops. For very large  $We_0$  values, very large  $Re_0$  values are expected, which would make the external flow more chaotic, which can have a major impact on the pressure forces experienced by the drop, its interaction with downstream vortices, and intensity of surface waves (section 3.2). These effects have not been taken into account in our derivation of  $C_{breakup}$ .

For the non-dimensional parameter space considered in the current work,  $C_{breakup}$  captures the dominant physics very well and succeeds in compressing the rather large variance in  $We_{cr}$  values observed due to very low  $\rho$  and high  $Oh_d$  and  $Oh_o$  values. Therefore, for the purposes of the work,  $C_{breakup}$  fulfills our requirements.

## 5. Conclusions

The current work aimed to clarify two major questions: **1.** The effect of  $We_0$ ,  $\rho$ ,  $Oh_o$  and  $Oh_d$  on drop deformation and breakup characteristics, at or near the  $We_{cr}$  and for physical properties that are vastly different from commonly available water-air systems; and **2.** The effect of these non-dimensional parameters on drop critical breakup morphology. As has been explained extensively in section 1, most of the currently accepted ideas on critical secondary atomization, such as the independence of  $We_{cr}$  with

respect to  $Oh_d$  given it is below 0.1, or the critical breakup morphology being solely a backward bag, etc. originate from experimental works done for a small parametric space occupied by water-air analogous systems. The current work aimed to shed some light on these accepted ideas and provide a more complete picture of the process of secondary atomization of Newtonian drops. For this purpose, a parametric sweep across all the involved non-dimensional parameters, i.e.  $\{\rho, Oh_o, Oh_d\}$  (section 2.4) was performed using axisymmetric simulations on Basilisk, with  $We_0$  values increased until a non-vibrational (critical) breakup was achieved for a given  $\{\rho, Oh_o, Oh_d\}$  set. From the subsequently obtained simulation results, the effect of each of the non-dimensional parameters on a drop deformation were characterized and related to the external forces acting on the drop and the corresponding internal flows (section 3).  $We_{cr}$  for the parameter space was obtained and plotted against  $Oh_d$  (figure 16) to recreate the plot presented in Hsiang & Faeth (1995). Based on all the analysis performed on the simulation results, a phase diagram (figure 17) was constructed describing the various deformation pathways of a spherical drop under impulsive acceleration depending on the properties. The simulations also allowed us to explore bag inflation characteristics for backward bag breakups for a greater parameter space, and extract some general conclusions on the associated timescales and growth rates. Additionally,  $t^* \approx 1$  was found to be a good measure for the timescale required for the initiation of bag inflation. Finally, a non-dimensional parameter ( $C_{breakup}$ ) was derived to provide a more complete alternative to Weber number as an indicator of drop threshold criteria in the dimensional space of the current study, by capturing the effects of all three studied non-dimensional parameters, i.e.,  $\rho$ ,  $Oh_o$ , and  $Oh_d$ , on drop deformation and breakup.

## 6. Acknowledgment

Computational resources provided by the Covid-19 HPC Consortium through time on Blue Waters (NCSA) were used for the simulations. S.D. and A.P.’s participation was supported by the DOE Office of Science through the National Virtual Biotechnology Laboratory (NVBL), a consortium of DOE national laboratories focused on response to COVID-19, with funding provided by the Coronavirus CARES Act.

## Appendix A. Numerical Scheme

Basilisk solves incompressible Navier Stokes multiphase flow equations (A 1 A 2 & A 3) on a quad/octree discretized grid, which allows variable mesh densities at the interface (Popinet 2003) and therefore accurately capture capillary scale phenomena.

$$\rho(\partial_t \mathbf{u} + \mathbf{u} \cdot \nabla \mathbf{u}) = -\nabla p + \nabla \cdot (2\mu \mathbf{D}) + \sigma \kappa \delta_s \mathbf{n}, \quad (\text{A } 1a)$$

$$\partial_t \rho + \nabla \cdot (\rho \mathbf{u}) = 0, \quad (\text{A } 1b)$$

$$\nabla \cdot \mathbf{u} = 0 \quad (\text{A } 1c)$$

where  $\mathbf{u} = (u, v, w)$  is the fluid velocity,  $\rho \equiv \rho(\mathbf{x}, t)$  is the fluid density,  $\mu \equiv \mu(\mathbf{x}, t)$  is the dynamic viscosity, and  $\mathbf{D}$  is the deformation tensor defined as  $D_{ij} = (\partial_i u_j + \partial_j u_i)/2$ . The Dirac distribution function  $\delta_s$  allows inclusion of surface tension forces in the momentum equation by switching on the surface tension term only at the interface between the fluids;  $\sigma$  is the surface tension coefficient,  $\kappa$  and  $\mathbf{n}$  the curvature and the normal to the interface, respectively.  $\kappa$  is computed using Height Function (HF) formulation as described by Torrey *et al.* (1985), with attention given to address under-resolved interfaces. The surface tension term is calculated using Continuum Surface Force (CSF) approach first described

in Brackbill *et al.* (1992), with special care taken to ensure that the conditions described in Francois *et al.* (2006) are satisfied to prevent parasitic currents.

To maintain the single equation formulation of the momentum equation, the two fluids are represented using a volume fraction  $c(\mathbf{x}, t)$  according to which  $\rho$  and  $\mu$  are defined as:

$$\rho = c\rho_1 + (1 - c)\rho_2, \quad (\text{A } 2a)$$

$$\mu = c\mu_1 + (1 - c)\mu_2 \quad (\text{A } 2b)$$

$\rho_1, \rho_2$  and  $\mu_1, \mu_2$  are the densities of the first and second fluid in the domain, respectively. In this formulation, the density advection equation is replaced with a volume fraction advection equation:

$$\partial_t c + \nabla \cdot (c\mathbf{u}) = 0 \quad (\text{A } 3)$$

The entire computational domain is discretized using squares for 2D (quadtrees) and cubes for 3D (octrees) and then organized in a hierarchy of cells. The mesh resolution is adaptive in nature, and hence the two-fluid interface is resolved at a much higher resolution than other computationally less interesting regions of the domain. This allows for large savings in the computational costs for two-phase simulations. Any cell serving as a parent computational element can undergo further refinement into four or eight equal children cells for 2D and 3D computations, respectively. Each of the children cells, in turn, can act as a parent cell if further refinement is warranted. This successive refinement continues until a (user-defined) threshold criterion for error is satisfied or a maximum refinement level is reached. A wavelet-based error estimation is used to estimate errors associated with the specified fields (Popinet 2015). The maximum allowed refinement, corresponding to the smallest allowed cell size, is constrained by a user-specified minimum allowed cell dimension, which is defined by a parameter called ‘‘Maximum Level’’, a maximum level of  $N$  corresponding to a minimum cell size of  $L/2^N$ .

## Appendix B. Numerical Convergence of Simulation Results

Before using Basilisk for the production runs, it is essential to test convergence of the numerical scheme with regards to both the maximum mesh resolution (normally achieved at the interface) and Wavelet-error thresholds for the specified field variables. For drop simulations, the accuracy of the calculated interface and the velocity fields must be ensured for correct retrieval of surface stresses, and correspondingly the temporal development of drop deformation process. Hence in the current simulations, the extent of adaptive mesh refinement performed at a computational cell is restricted by the allowable maximum errors for velocity ( $u_e$ ) and volume fraction ( $c_e$ ) fields. Additionally, a maximum allowed refinement level ( $N$ ) is specified which enforces a strict minimum cell size of  $L/2^N$  across all the computational cells. This helps prevent unbounded mesh refinement if the error threshold criteria converges slowly with decrease in cell size in a computational cell, which in turn eases the restriction on simulation timestep (dependent on the cell with the highest CFL number in the domain).

To test the convergence of the axisymmetric simulations performed in Basilisk with respect to these parameters, we simulate multiple cases with varying  $u_e$ ,  $c_e$  and  $N$ , and fixed physical properties of  $\{\rho, Oh_o, Oh_d, We_0\} = \{500, 0.01, 0.1, 16\}$  on an axisymmetric domain (figure 2) with  $L = 16$ ,  $D = 1$  and  $V_0 = 1$ . A drop-ambient system with these physical properties is expected to show a bag breakup and hence provides a good representative case for these grid independence tests. The corresponding convergence plots are shown in figure 20.

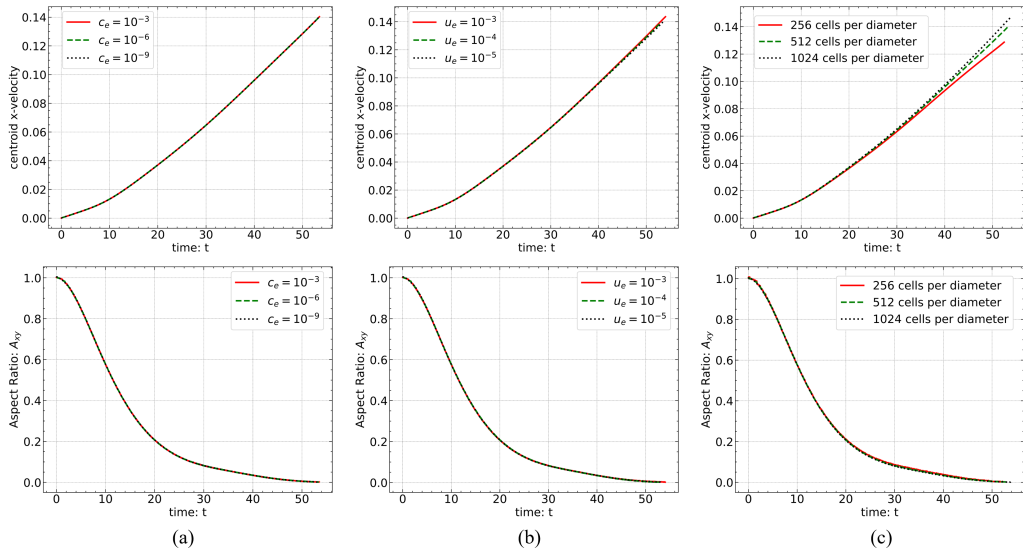


FIGURE 20. Tests of convergence plots for the choice of wavelet based error thresholds for (a)  $c$  and (b)  $\mathbf{u}$  are shown. In (c), mesh convergence with respect to the maximum allowed refinement  $2^N/L$  is plotted. 256, 512 and 1024 cells per diameter correspond to  $N = 12$ ,  $N = 13$ , and  $N = 14$  respectively, given  $L = 16$  and  $D = 1$ .

In figure 20(a), we observe that all  $c_e$  values from  $10^{-3}$  to  $10^{-9}$  show essentially identical x-velocities and aspect ratios. The increase in computational costs for a  $10^{-3}$  factor decrease in  $f_e$  is very small and hence allows the large jumps (multiples of  $10^{-3}$ ) in consecutive values of  $c_e$  for the grid independence tests. A  $c_e$  of  $10^{-6}$  is chosen as the threshold error for  $c$ .

Figure 20(b) plots convergence tests with respect to  $\mathbf{u}_e$ . x-velocities corresponding to all the three values of  $u_e$  show negligible differences, where as the computational cost shows jump of approximately 2.5 times from  $u_e = 10^{-4}$  to  $u_e = 10^{-5}$ . Hence,  $u_e = 10^{-4}$  is chosen for the production runs.

Finally from the convergence plot in figure 20(c), it is evident that the effect of  $N$  on x-velocities is significant.  $N$  also has a dramatic effect on computational costs, with  $N = 14$  requiring approximately 3 times the computational time as required for  $N = 13$ .  $N = 13$ , which is equivalent to 512 cells per diameter for  $L = 16$ , provides a good balance between accuracy and computational costs. This resolution is used for all cases except for the highest  $Re_0$  cases ( $Oh_o = 0.0001$ ) which require a (higher) maximum cell resolution of 1024 cells per diameter.

## Appendix C. Comparison to 3D simulations

To further justify the use of axisymmetric simulations in this study, Basilisk is used to conduct both 3D and axisymmetric simulations for multiple low density-ratio drops. Simulations have been limited to low density ratio values since high  $\rho$  3D simulations are computationally not feasible given the available computational resources. Moreover, as stated by Jain *et al.* (2019), “For the drops with high  $\rho$ , flow around the drop has relatively low effect on the drop deformation, morphology and the breakup.” This insight reinforces the decision of concentrating on low-density ratio cases, where the influence of flow around the drop is more pronounced. We also choose low Outside Ohnesorge number values (high initial Reynolds number) to ensure that the ambient flow is in turbulent

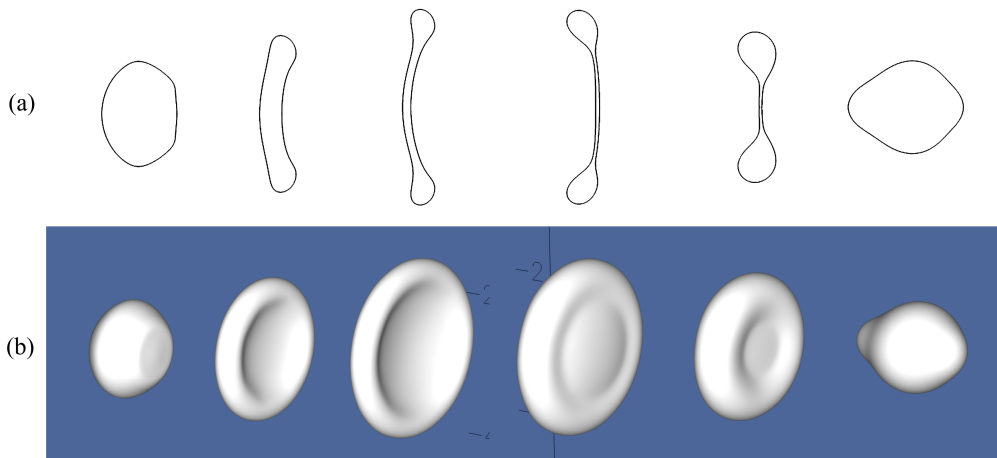


FIGURE 21. Images in (a) and (b) compare development of the fluid interface with time for axisymmetric and 3D simulations respectively for a case with  $\rho = 50$ ,  $Oh_o = 0.001$ ,  $Oh_d = 0.1$ ,  $We_0 = 17$ . The inflow is from left to right, and the corresponding drop deformation is arranged in the same direction.

regime. This choice renders the ambient flow non-axisymmetric since the formation of turbulent vortices is a purely 3D phenomenon, making such a flow system in theory difficult to perfectly reproduce with only axisymmetric simulations. Consequently, low density-ratio cases in high  $Re_0$  flows are expected to best highlight all the differences (if any) in the macroscopic properties associated with the drop between axisymmetric and full 3D simulations.

The comparison of fluid interface evolution with time between 3D and axisymmetric simulations is illustrated in figure 21 for a specific case with  $\{\rho, Oh_o, Oh_d, We_0\} = \{50, 0.001, 0.1, 17\}$ . Under the action of a uniform ambient inflow, the drop undergoes deformation with time as shown through a series of VoF plots from left to right. We observe that the various stages of drop deformation, from a forward-facing pancake (col. 2), to a forward-facing bag (col. 3), to its flipping to a backward bag (col. 3-4), are accurately captured by axisymmetric simulations.

Figure 22 plots centroid x-velocity and aspect ratio for the three different cases. Both 3D and axisymmetric cases show extremely similar aspect ratios and x-velocities for the majority of the process. Differences start to emerge only as the drops reach their lowest aspect ratios and start oscillating back to the equilibrium spherical shape, represented by the increasing  $A_{xy}$  (figure 22(a)). This deviation in  $A_{xy}$  beyond the time of minimum  $A_{xy}$ , equivalent to the differences in frontal areas, results in diverging centroid x-velocities between axisymmetric and 3D simulations, as can be observed from figure 22(b).

However, these differences are inconsequential when the broader deformation characteristics of a drop are concerned, i.e. the pancake shape and the general breakup morphology. Furthermore, once the drop attains its maximum deformation state without fragmentation, its primary deformation process (driven by impulsive acceleration) is complete. Subsequent retraction to its equilibrium spherical shape would be accompanied by continuous energy dissipation due to viscosity, resulting in the drop never matching the minimum  $A_{xy}$  value attained during its primary deformation. Therefore, for the purposes of this work, axisymmetric simulations are considered adequate since our focus is on this primary deformation during the initial half-oscillation time period. As discussed in the

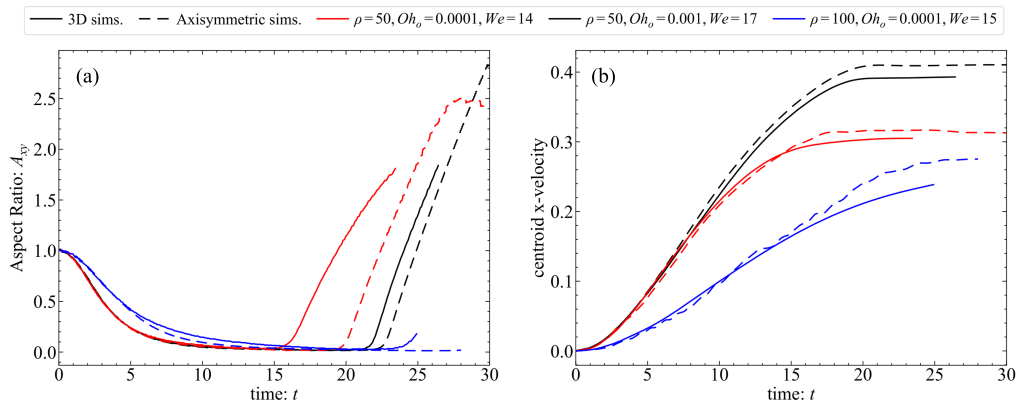


FIGURE 22. All cases have  $Oh_d = 0.1$  and other non-dimensional parameters as listed in the plots. (a) shows the variation of drop Aspect Ratio with time, (b) shows the variation of centroid x-velocity with time, for axisymmetric and 3D simulations.

preceding section, the final breakup of a drop almost always is a sheet breakup which is driven by non-axisymmetric surface instabilities (e.g. Rayleigh-Plateau instability for rupture of bag), making accurate estimation of statistics such as drop size distribution, the bag size, breakup time, instantaneous velocity during the time of breakup, etc., not achievable through axisymmetric simulations. Nevertheless, for the current study, these statistics are not within the scope of interest.

## REFERENCES

- BATCHELOR, GEORGE KEITH 1967 *An introduction to fluid dynamics*. Cambridge university press.
- BLACKWELL, BRENDAN C., DEETJEN, MARC E., GAUDIO, JOSEPH E. & EWOLDT, RANDY H. 2015 Sticking and splashing in yield-stress fluid drop impacts on coated surfaces. *Physics of Fluids* **27** (4), 043101, publisher: American Institute of Physics.
- BRACKBILL, J. U., KOTHE, D. B & ZEMACH, C 1992 A continuum method for modeling surface tension. *Journal of Computational Physics* **100** (2), 335–354.
- BREMOND, N. & VILLERMAUX, E. 2005 Bursting thin liquid films. *Journal of Fluid Mechanics* **524**, 121–130, publisher: Cambridge University Press.
- CAO, XIAN KUI, SUN, ZHI GANG, LI, WEI FENG, LIU, HAI FENG & YU, ZUN HONG 2007 A new breakup regime of liquid drops identified in a continuous and uniform air jet flow. *Physics of Fluids* **19** (5), 057103.
- DAI, Z. & FAETH, G. M. 2001 Temporal properties of secondary drop breakup in the multimode breakup regime. *International Journal of Multiphase Flow* **27** (2), 217–236.
- DEVILLE, MICHEL O, FISCHER, PAUL F & MUND, ERNEST H 2002 *High-order methods for incompressible fluid flow*, , vol. 9. Cambridge university press.
- DIMOTAKIS, PAUL E 1986 Two-dimensional shear-layer entrainment. *AIAA journal* **24** (11), 1791–1796.
- DORSCHNER, BENEDIKT, BIASIORI-POULANGES, LUC, SCHMIDMAYER, KEVIN, EL-RABII, HAZEM & COLONIUS, TIM 2020 On the formation and recurrent shedding of ligaments in droplet aerobreakup. *Journal of Fluid Mechanics* **904**, publisher: Cambridge University Press.
- FLOCK, A.K., GULDENBECHER, D.R., CHEN, J., SOJKA, P.E. & BAUER, H.-J. 2012 Experimental statistics of droplet trajectory and air flow during aerodynamic fragmentation of liquid drops. *International Journal of Multiphase Flow* **47**, 37–49, publisher: Pergamon.
- FOROUZI FESHALAMI, BEHZAD, HE, SHUISHENG, SCARANO, FULVIO, GAN, LIAN & MORTON,

- CHRIS 2022 A review of experiments on stationary bluff body wakes. *Physics of Fluids* **34** (1), 011301, publisher: American Institute of Physics.
- FRANCOIS, MARIANNE M., CUMMINS, SHAREN J., DENDY, EDWARD D., KOTHE, DOUGLAS B., SICILIAN, JAMES M. & WILLIAMS, MATTHEW W. 2006 A balanced-force algorithm for continuous and sharp interfacial surface tension models within a volume tracking framework. *Journal of Computational Physics* **213** (1), 141–173.
- FUSTER, DANIEL, AGBAGLAH, GILOU, JOSSERAND, CHRISTOPHE, POPINET, STÉPHANE & ZALESKI, STÉPHANE 2009 Numerical simulation of droplets, bubbles and waves: State of the art. *Fluid Dynamics Research* **41** (6), 065001.
- GELFAND, B E 1996 Droplet breakup phenomena in flows with velocity lag. *Progress in Energy and Combustion Science* **22** (3), 201–265.
- GOODRIDGE, CHRISTOPHER L., SHI, W. TAO, HENTSCHEL, H. G. E. & LATHROP, DANIEL P. 1997 Viscous effects in droplet-ejecting capillary waves. *Physical Review E* **56** (1), 472–475, publisher: American Physical Society.
- GULDENBECHER, D. R., LÓPEZ-RIVERA, C. & SOJKA, P. E. 2009 Secondary atomization. *Experiments in Fluids* **46** (3), 371–402, publisher: Springer.
- HAN, JAEHOON & TRYGGVASON, GRETAR 2001 Secondary breakup of a axisymmetric liquid drops. II. Impulsive acceleration. *Physics of Fluids* **13** (6), 1554–1565, publisher: American Institute of PhysicsAIP.
- HINZE, J. O. 1949 Critical speeds and sizes of liquid globules. *Applied Scientific Research* **1** (1), 273–288.
- HINZE, J. O. 1955 Fundamentals of the hydrodynamic mechanism of splitting in dispersion processes. *AIChE Journal* **1** (3), 289–295.
- HSIANG, LP & FAETH, GM 1995 Drop deformation and breakup due to shock wave and steady disturbances. *International Journal of Multiphase Flow* **21** (4), 545–560.
- HSIANG, L. P. & FAETH, G. M. 1992 Near-limit drop deformation and secondary breakup. *International Journal of Multiphase Flow* **18** (5), 635–652.
- JACKIW, ISAAC M. & ASHGRIZ, NASSER 2021 On aerodynamic droplet breakup. *Journal of Fluid Mechanics* **913** (A33), 1–46.
- JAIN, MOHIT, PRAKASH, R. SURYA, TOMAR, GAURAV & RAVIKRISHNA, R. V. 2015 Secondary breakup of a drop at moderate Weber numbers. *Proceedings of the Royal Society A: Mathematical, Physical and Engineering Sciences* **471** (2177), publisher: Royal Society of London.
- JAIN, SUHAS S., TYAGI, NEHA, PRAKASH, R. SURYA, RAVIKRISHNA, R. V. & TOMAR, GAURAV 2019 Secondary breakup of drops at moderate Weber numbers: Effect of Density ratio and Reynolds number. *International Journal of Multiphase Flow* **117**, 25–41, arXiv: 1803.02989 Publisher: Elsevier Ltd.
- JALAAL, M. & MEHRAVARAN, K. 2012 Fragmentation of falling liquid droplets in bag breakup mode. *International Journal of Multiphase Flow* **47**, 115–132, publisher: Pergamon.
- JALAAL, M. & MEHRAVARAN, K. 2014 Transient growth of droplet instabilities in a stream. *Physics of Fluids* **26** (1), 012101, publisher: American Institute of Physics.
- KARAM, H. J. & BELLINGER, J. C. 1968 Deformation and Breakup of Liquid Droplets in a Simple Shear Field. *Industrial & Engineering Chemistry Fundamentals* **7** (4), 576–581, publisher: American Chemical Society.
- KHOSLA, SACHIN & SMITH, CLIFFORD E 2006 Detailed Understanding of Drop Atomization by Gas Crossflow Using the Volume of Fluid Method. In *ILASS Americas, 19th Annual Conference on Liquid Atomization and Spray Systems*. Institute for Liquid Atomization and Spray Systems.
- KRZECZKOWSKI, STEFAN A. 1980 Measurement of liquid droplet disintegration mechanisms. *International Journal of Multiphase Flow* **6** (3), 227–239, publisher: Pergamon.
- KULKARNI, V. & SOJKA, P. E. 2014 Bag breakup of low viscosity drops in the presence of a continuous air jet. *Physics of Fluids* **26** (7), 072103, publisher: American Institute of Physics.
- LOZANO, ANTONIO, GARCÍA-OLIVARES, ANTONIO & DOPAZO, CÉSAR 1998 The instability growth leading to a liquid sheet breakup. *Physics of Fluids* **10** (9), 2188–2197.
- MARCOTTE, FLORENCE & ZALESKI, STÉPHANE 2019 Density contrast matters for drop

- fragmentation thresholds at low Ohnesorge number. *Physical Review Fluids* **4** (10), 103604, publisher: American Physical Society.
- PILCH, M. & ERDMAN, C.A. 1987 Use of breakup time data and velocity history data to predict the maximum size of stable fragments for acceleration-induced breakup of a liquid drop. *International Journal of Multiphase Flow* **13** (6), 741–757, publisher: Pergamon.
- POPINET, STÉPHANE 2003 Gerris: a tree-based adaptive solver for the incompressible Euler equations in complex geometries. *Journal of Computational Physics* **190** (2), 572–600, publisher: Academic Press.
- POPINET, STÉPHANE 2009 An accurate adaptive solver for surface-tension-driven interfacial flows. *Journal of Computational Physics* **228** (16), 5838–5866, publisher: Academic Press.
- POPINET, STÉPHANE 2015 A quadtree-adaptive multigrid solver for the Serre–Green–Naghdi equations. *Journal of Computational Physics* **302**, 336–358, publisher: Elsevier.
- PRUPPACHER, H. R. & BEARD, K. V. 1970 A wind tunnel investigation of the internal circulation and shape of water drops falling at terminal velocity in air. *Quarterly Journal of the Royal Meteorological Society* **96** (408), 247–256, publisher: John Wiley & Sons, Ltd.
- RIMBERT, N., CASTRILLON ESCOBAR, S., MEIGNEN, R., HADJ-ACHOUR, M. & GRADECK, M. 2020 Spheroidal droplet deformation, oscillation and breakup in uniform outer flow. *Journal of Fluid Mechanics* **904**, 15–16, publisher: Cambridge University Press.
- SZAKÁLL, MIKLOÓS, DIEHL, KAROLINE & MITRA, SUBIR K. 2009 A wind tunnel study on the shape, oscillation, and internal circulation of large raindrops with sizes between 2.5 and 7.5 mm. *Journal of the Atmospheric Sciences* **66** (3), 755–765.
- THEOFANOUS, T.G. 2011 Aerobreakup of Newtonian and Viscoelastic Liquids. *Annual Review of Fluid Mechanics* **43** (1), 661–690, eprint: <https://doi.org/10.1146/annurev-fluid-122109-160638>.
- THEOFANOUS, T. G., LI, G. J. & DINH, T. N. 2004 Aerobreakup in Rarefied Supersonic Gas Flows. *Journal of Fluids Engineering* **126** (4), 516–527.
- TORREY, M. D., CLOUTMAN, L. D., MJOLSNESS, R. C. & HIRT, C. W. 1985 NASA-VOF2D: a computer program for incompressible flows with free surfaces. *NASA STI/Recon Technical Report N* **86**, 30116, aDS Bibcode: 1985STIN...8630116T.
- TURTON, R. & LEVENSPIEL, O. 1986 A short note on the drag correlation for spheres. *Powder Technology* **47** (1), 83–86.
- VILLERMAUX, E. 2007 Fragmentation. *Annual Review of Fluid Mechanics* **39** (1), 419–446, publisher: Annual Reviews.
- VILLERMAUX, EMMANUEL & BOSSA, BENJAMIN 2009 Single-drop fragmentation determines size distribution of raindrops. *Nature Physics* **5** (9), 697–702, publisher: Nature Publishing Group.
- WIERZBA, A. 1990 Deformation and breakup of liquid drops in a gas stream at nearly critical Weber numbers. *Experiments in Fluids* **9** (1), 59–64.
- ZHAO, HUI, LIU, HAI FENG, CAO, XIAN KUI, LI, WEI FENG & XU, JIAN LIANG 2011 Breakup characteristics of liquid drops in bag regime by a continuous and uniform air jet flow. *International Journal of Multiphase Flow* **37** (5), 530–534, publisher: Pergamon.